High-Performance Negative Self-Powered α-MoO_3/Ir/α-MoO_3 Photodetectors Probing the Influence of Coulomb Deep Traps

Basyooni, Mohamed A.; Tihtih, Mohammed; Zaki, Shrouk E.; Eker, Yasin Ramazan

DOI
10.1021/acsaelm.3c01047

Publication date
2023

Document Version
Final published version

Published in
ACS Applied Electronic Materials

ACS APPLIED ELECTRONIC MATERIALS

pubs.acs.org/acsaelm Article

High-Performance Negative Self-Powered α-MoO_3/Ir/α-MoO_3 Photodetectors: Probing the Influence of Coulomb Deep Traps

Mohamed A. Basyooni,* Mohammed Tihtih, Shrouk E. Zaki, and Yasin Ramazan Eker

Cite This: *ACS Appl. Electron. Mater.* 2023, 5, 5696−5713 Read Online

ACCESS | Metrics & More | Article Recommendations | Supporting Information

ABSTRACT: Nanostructures of ultrathin 2D MoO_3 semiconductors have gained significant attention in the field of transparent optoelectronics and nanophotonics due to their exceptional responsiveness. In this study, we investigate self-powered α-MoO_3/Ir/α-MoO_3 photodetectors, focusing on the influence of induced hot electrons in ultrathin α-MoO_3 when combined with an ultrathin Ir plasmonic layer. Our results reveal the presence of both positive and negative photoconductivity at a 0 V bias voltage. Notably, by integrating a 2 nm Ir layer between post-annealed α-MoO_3 films, we achieve remarkable performance metrics, including a high I_{ON}/I_{OFF} ratio of 3.8×10^6, external quantum efficiency of 132, and detectivity of 3.4×10^{11} Jones at 0 V bias. Furthermore, the response time is impressively short, with only 0.2 ms, supported by an exceptionally low MoO_3 surface roughness of 0.1 nm. The observed negative photoresponse is attributed to O_2 desorption from the MoO_3 surface, resulting in increased carrier density and reduced mobility in the Ir layer due to Coulomb trapping and oxygen vacancy deep levels. Consequently, this leads to a decreased carrier mobility and diminished current in the heterostructure. Our findings underscore the enormous potential of ultrathin MoO_3 semiconductors for high-performance negative conductivity optoelectronics and photonic applications.

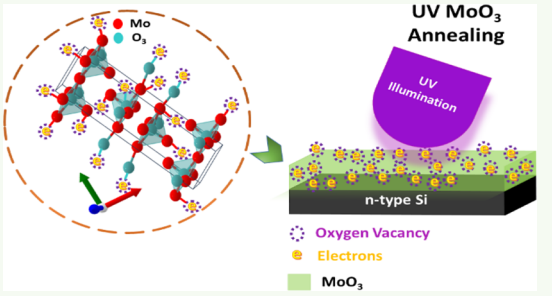

KEYWORDS: *MoO_3, iridium, plasmonics photodetectors, negative photoconductivity (NPC), atomic layer deposition (ALD)*

INTRODUCTION

In a semiconductor, the conductivity is determined by the movement of charge carriers, which are typically electrons and "holes" (positively charged vacancies left behind when electrons move). The conductivity of a semiconductor can be influenced by external factors like temperature, applied electric fields, and the presence of impurities or other materials.[1] Intrinsic photoconductivity primarily involves transitions of electrons from the valence band to the conduction band, driven by the absorption of light, while extrinsic photoconductivity involves charge carrier generation associated with impurity energy levels introduced through doping or defects in the semiconductor material. Both intrinsic and extrinsic photoconductivity play important roles in the behavior of semiconductors under light exposure and are crucial for various optoelectronic applications, such as solar cells, photodetectors, and imaging sensors.

Positive photoconductivity (PPC) refers to the increase in the conductivity that occurs when a semiconductor is illuminated. Conversely, negative photoconductivity (NPC) occurs when the conductivity decreases under illumination. The phenomenon of NPC has been detected in different semiconductor materials, and numerous theoretical models have been suggested in scientific literature to elucidate the underlying mechanism.[2−11] NPC can be attributed to the existence of an intense nonequilibrium electron distribution in the CB upon monoenergetic excitation. Under such circumstances, the lifetime of electrons in the CB is shorter than the relaxation time resulting from acoustic phonon scattering. As a consequence, when the energy of the photogenerated electrons is a multiple of the longitudinal optical phonon energy, the photocurrent generated flows in the opposite direction to the electric field.[6] The causes of NPC in various materials are diverse and can be attributed to different factors. These include the formation of scattering centers,[12,13] deep defect levels,[14] water adsorption,[15] surface plasmon resonance,[16] charge carrier trapping,[17] and donor atom-like centers,[18] among others. Some other possible reasons are the generation of secondary hot electrons,[12,13] the trionic effect,[19] the formation of the built-in-electric field,[20,21] light-activated trap states,[22] thermal broadening of electron distribution,[6] and intraband scattering.[23] However, despite numerous studies, there is still no clear consensus on the fundamental cause of this phenomenon.

In a study by Yang et al.,[24] they observed NPC in a MoO_3 nanoflakes/graphene heterocomposite under red light irradiation. The current flowing through the sample decreased to 10%

Received: August 3, 2023
Accepted: September 27, 2023
Published: October 4, 2023

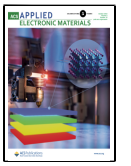

https://doi.org/10.1021/acsaelm.3c01047
ACS Appl. Electron. Mater. 2023, 5, 5696−5713

of its original value when exposed to red light, indicating an approximately 10-fold increase in resistance. The resistance recovery process took over 500 s, suggesting that restoring the original resistance was more challenging than the resistance increase. This negative photoconductivity behavior demonstrated the ability to control the resistance of the heterocomposite using red light irradiation, highlighting its potential for photoresponsive applications. In principle, both NPC and PPC could be observed in some materials under different conditions. PbTe, a well-studied semiconductor, exhibits both PPT and NPC. Introducing elements like Ga and Eu in the doping process of p-type $Pb_{1-x}Eu_xTe$ films triggers a transition from negative to positive photoconductivity. The disorder caused by Eu atoms leads to a metal−insulator transition known as the Anderson transition. The behavior is influenced by the position of the 4f level, and under illumination, positive photoconductivity arises from the involvement of the 4f level, while negative photoconductivity arises from defect levels within the energy gap.[25] In a separate investigation carried out by Grillo et al.,[26] both NPC and PPC were identified in $PtSe_2$ field-effect transistors. The researchers observed that the transition from PPC to NPC is contingent on environmental pressure. The pressure-dependent behavior of photoconductivity suggests that the adsorption and desorption of air molecules significantly influence the charge transport. When the light source is deactivated, an excess of electron−hole recombination induces a decrease in current, followed by a gradual increase in current due to the readsorption of oxygen on the surface of $PtSe_2$. By comprehending the charge transfer dynamics between physisorbed oxygen molecules and the $PtSe_2$ layer, a novel avenue emerges for controlling carrier density and the optical properties of the material.[27]

NPC devices have a wide range of potential applications. They can be used in photodetection and imaging, allowing for highly sensitive imaging under low-light conditions, night vision technology, and improved astronomical observations. NPC devices also serve as optoelectronic switches. This makes them useful in optical communication systems, where fast data transmission is required. In the field of photovoltaics, NPC materials can be integrated into solar cells to enhance efficiency by reducing power losses under intense light. Additionally, NPC devices can be utilized as light sensors or light-dependent resistors (LDRs). They have applications in automatic brightness control for displays, adaptive street lighting, and proximity sensors. Lastly, NPC materials show promise in optical memory devices, enabling the storage and retrieval of data using light. Qin et al. and Zhuang et al. have demonstrated the use of NPC in nanodiamonds and applied it to high-sensitivity carbon-based humidity sensors.[28,29] Hassan et al. observed NPC in HfO_x thin films and used it for visible light sensors.[30] Similarly, Singh et al. utilized the NPC concept for CuSe photodetector (PD) and achieved a sensitivity of 618 A/W under low bias.[31] Moreover, the NPC phenomenon has been applied in ultraresponsive PD applications, including $Cr_2Ge_2Te_6$ and $Cs_3Bi_2Cl_9$ single crystals-based PD.[21,32] These detectors showed high responsivity and on−off ratios. Additionally, NPC can be used for space exploration as doped semiconductors can exhibit ultraresponsive NPC, and the detection wavelength can be tuned in the infrared region by using different dopants.[29,33] Overall, NPC devices have diverse applications and offer exciting possibilities for various technological advancements.

Gibbs free energy of IrO_2 is reported before,[34] it is worth noting that 1T-IrO_2 exhibits remarkable durability, with minimal degradation even after undergoing an exhaustive 126 h chronopotentiometry measurement under the demanding conditions of a high current density of 250 mA/cm^2 within a proton exchange membrane device. This impressive resilience underscores its potential for enduring high-performance applications. Thus, IrO_2 stands out as the sole recognized catalyst for the oxygen evolution reaction (OER) that possesses a combination of remarkable catalytic activity and enduring stability in acidic environments.[35] This study investigates the integration of ultrathin plasmonic Ir films (1, 2, and 4 nm) within a MoO_3−MoO_3 sandwich structure on a Silicon substrate. Post-annealing processes are applied to the samples. Optoelectronic properties under UV illumination and at 0 V bias conditions will be examined for self-powered UV PD. Hall effect measurements will determine carrier concentration and mobility, indicating performance factors such as responsitivity (P_g), detectivity (D^*), external quantum efficiency (EQE), and OFF-ON responses. Overall, these findings demonstrate the potential of using nanostructured MoO_3/Ir heterostructures for high-performance self-powered PDs. By understanding the underlying mechanisms governing optoelectronic behaviors and the role of specific layers, we can further optimize the design and performance of these devices. The study will also analyze the influence of the plasmonic Ir layer on electron/hole concentrations and provide insights into the observed negative photoconductivity phenomena.

MATERIALS AND METHODS

Preparing the Ultrathin MoO_3 Film. A 2D α-MoO_3 film was synthesized on a 1 cm^2 n-type Si substrate by using an ALD system. To activate the substrate surface, an O_2 plasma cleaner was employed for 1 min. Subsequently, the substrate was placed in the ALD chamber for the growth of the MoO_3 thin film using the ANRIC Technologies brand (AT410) ALD system. For the deposition process, a Mo-based organometallic precursor material, bis(*t*-butylimido)bis(dimethylamino)-molybdenum(VI), was introduced onto the substrate surface within an argon atmosphere of 99.999% purity, with a flow rate of 20 sccm, under a low pressure of approximately 0.3 Torr. The amount of precursor material deposited was controlled by adjusting the open time of the valve between the growth chamber and the precursor material chamber as well as the temperature of the growth chamber and the controlled heating of the precursor material chamber (∼80 °C). To prevent condensation between the growth chamber and the material chamber, the pipes were maintained at 100 °C, while the outlet manifold was kept at 105 °C. In the subsequent stage, the gases released during deposition on the substrate were expelled from the growth chamber at a flow rate of 10 sccm. In the third stage, the controlled introduction of O_3 into the growth chamber was facilitated using the ANRIC Technology ATO_3 module. This oxidation process transformed the organo-metallic layer into a single layer of a MoO_3 thin film. Finally, the residual gases were evacuated to complete the cycle. Previous research has demonstrated that depositing MoO_3 samples at 200 °C yields favorable results for optoelectronic and electronic applications.[25]

Ultrathin Ir Layer. To achieve an ultrathin layer of Ir with a thickness of just a few nanometers, a Leica EM ACE600 US sputter coater was utilized. The objective was to examine the influence of Ir, so layers with thicknesses of 1, 2, and 4 nm were deposited while maintaining a constant thickness for the MoO_3 layer. The deposition took place on a high vacuum film surface under a pressure of 1×10^{-3} mbar. The deposition process involved the use of Ar plasma with a depositing pressure of 5.0×10^{-2} mbar and an applied current of approximately 50 mA. To monitor the thickness, a quartz thickness monitor was employed. The sputtering rate for all of the samples remained consistent at 0.06 nm/s. However, to enhance the crystallinity of the thin films and achieve the α-MoO_3 phase, it is advisable to subject the deposited MoO_3/Si to annealing in a tube furnace at 600 °C for 15

https://doi.org/10.1021/acsaelm.3c01047
ACS Appl. Electron. Mater. 2023, 5, 5696−5713

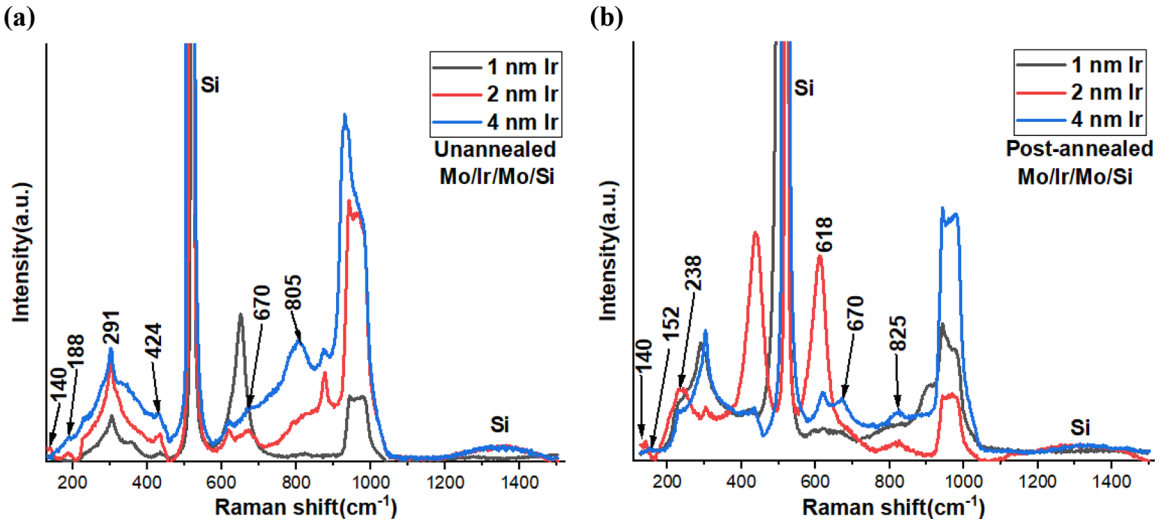

Figure 1. Raman spectroscopy analysis of unannealed (a) and post-annealed (b) MoO_3/Ir/MoO_3/Si with different thicknesses of the Ir layer of 1, 2, and 4 nm.

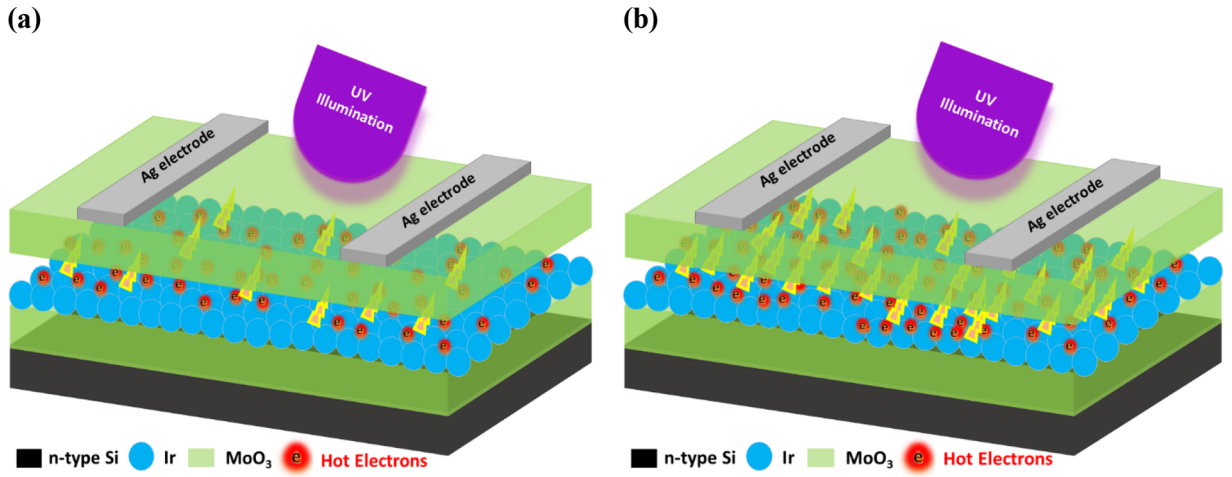

Figure 2. Schematic diagram for both unannealed (a) and post-annealed (b) samples under UV illumination.

min within an ambient air environment.[36,37] Following the annealing process, the Ir layer is deposited followed by the upper MoO_3 layer. For the unannealed samples, only the first MoO_3 layer was annealed, while the upper MoO_3 layer did not undergo annealing. In contrast, for the post-annealed samples, both the upper and lower MoO_3 layers received annealing under the same conditions.

Characterization Methods. A variety of characterization techniques were employed to understand the properties of the thin films. The surface morphology was analyzed by using a field-emission scanning electron microscope (FESEM) Zeiss Gemini 500, while energy-dispersive X-ray spectroscopy (EDS) was used to identify the elemental composition of the films. Atomic force microscopy (AFM) Park XE7 system was used to investigate the topography and line profile spectrum, and Raman spectroscopy of $\lambda = 532$ nm was used to study the crystallinity and identify the 2D α-MoO_3 phase. Electrical properties, including carrier concentration and mobility, were measured by using the SWIN Hall8800 Hall effect measurement system. Electrical I–V and optoelectronic measurements were performed by using a Sourcemeter and a four-probe system. The illumination source had a 365 nm UV wavelength. Finally, the thickness of the films was measured by using the FILMETRIC F20–UV thin film analyzer. The opportunity to analyze the diffuse reflectance (R) spectra of our prepared samples within the 200–700 nm range was facilitated by employing UV–vis-NIR Spectroscopy (UV-3600Plus, Shimadzu).

RESULTS AND DISCUSSION

Identifying the 2D α-MoO_3 Phase Raman Analysis. For a better understanding of the phase changes in the postannealed samples, we did a Ramana analysis for unannealed and postannealed samples and reported them in Figure 1. For the case of unannealed samples, it is seen that the main peak of 522 cm^{-1} is related to Si.[38] Meanwhile, by coating Ir, the MoO_3 Raman shift peaks predominated. The peaks at 522, 424, and 825 cm^{-1} are related to α-MoO_3. It can be seen that this shift to a higher Ramana shift is related to the thickness of Ir under MoO_3 film.[38] The introduction of an Ir layer, being a plasmonic metal, can significantly influence the Raman peaks due to its ability to enhance light reflection compared with the MoO_3 oxide layer. While 618, 617, and 618 cm^{-1} are associated with Si, 370 cm^{-1} corresponds to the α-MoO_3. The peaks of 822, 825, and 824 cm^{-1} could be related to Ir.[39] The peak at 1301 cm^{-1} is related to Si. Here, due to using two layers of MoO_3 in between Ir one, we found some more peaks related to MoO_3 at around 152, 140, and 188 cm^{-1}, respectively, for 1, 2, and 4 nm Ir thickness cases. However, the peak at 725 cm^{-1} might be related to Ir phase.[40] The peak at 816 cm^{-1} is attributed to 2D α-MoO_3.[41−43] Meanwhile, for the postannealed case, the Raman spectrum

https://doi.org/10.1021/acsaelm.3c01047
ACS Appl. Electron. Mater. 2023, 5, 5696−5713

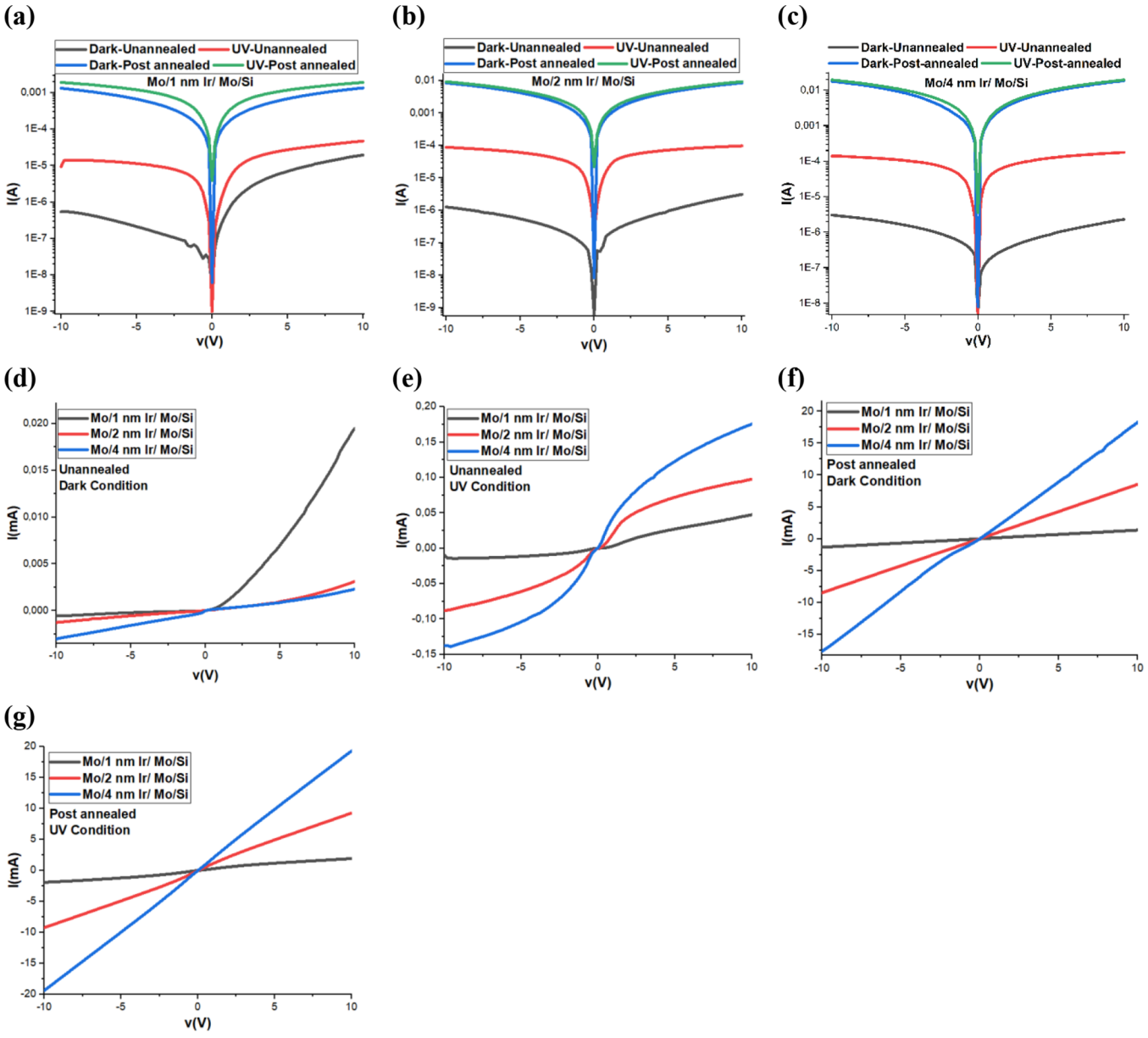

Figure 3. Log $I-V$ curves of Mo/Ir/Mo/Si samples with different Ir layer thicknesses: 1 nm (a), 2 nm (b), and 4 nm (c), considering both unannealed and postannealed films. Additionally, linear $I-V$ curves are provided for 1, 2, and 4 nm Ir thickness samples in both unannealed (d and e) and post-annealed (f and g) states.

shows interesting results. For the MoO_3/1 nm Ir/MoO_3/Si: 818 cm^{-1} is assigned to the A_{1g} mode,[44] and 291 and 669 cm^{-1} are assigned to the B_{2g} mode.[44] These are related to the 2D α-MoO_3 behavior. For MoO_3/2 nm Ir/MoO_3/Si: 823 cm^{-1} is assigned to the A_{1g} mode,[44] and 670 cm^{-1} is assigned to the B_{2g} mode,[44] which are also related to 2D α-MoO_3 behavior. The peak at 238 cm^{-1} corresponds to a nonstoichiometric MoO_{3-x}.[45] For MoO_3/4 nm Ir/MoO_3/Si: 826 cm^{-1} is assigned to the A_{1g} mode,[44] and 672 cm^{-1} is assigned to the B_{2g} mode.[44] These peaks are related to 2D α-MoO_3 behavior. Ultimately, the post-annealed MoO_3/2 nm Ir/MoO_3/Si sample exhibits heightened peak intensities, accompanied by intriguing peaks associated with the presence of a highly crystalline 2D α-MoO_3 film. This result could contribute to high optoelectronic performances and high carrier concentrations.

Current–Voltage Characteristics. The optoelectronic behavior under UV illuminations for both unannealed and postannealed samples promises an excitation of the hot electrons on the surface of the Ir layer. For this purpose, a schematic diagram representing the concentration of the hot electrons for unannealed and postannealed cases is depicted in Figure 2.

The logarithmic IV curves are shown in Figure 3a–c. A discernible presence of a minor current near the origin point was evident across all samples regardless of the Ir thickness. This subtle current persisted uniformly, irrespective of variations in the material. However, the distinction between samples subjected to light exposure and those in darkness was noteworthy. When the samples were examined under unilluminated conditions, the dark current remained notably low. This indicated that in the absence of light, the current near the origin point exhibited stability. Conversely, in the presence of illumination, a significant alteration became apparent. The dark current, which was initially at a minimum, displayed a noticeable increase when exposed to light. This alteration

https://doi.org/10.1021/acsaelm.3c01047
ACS Appl. Electron. Mater. 2023, 5, 5696−5713

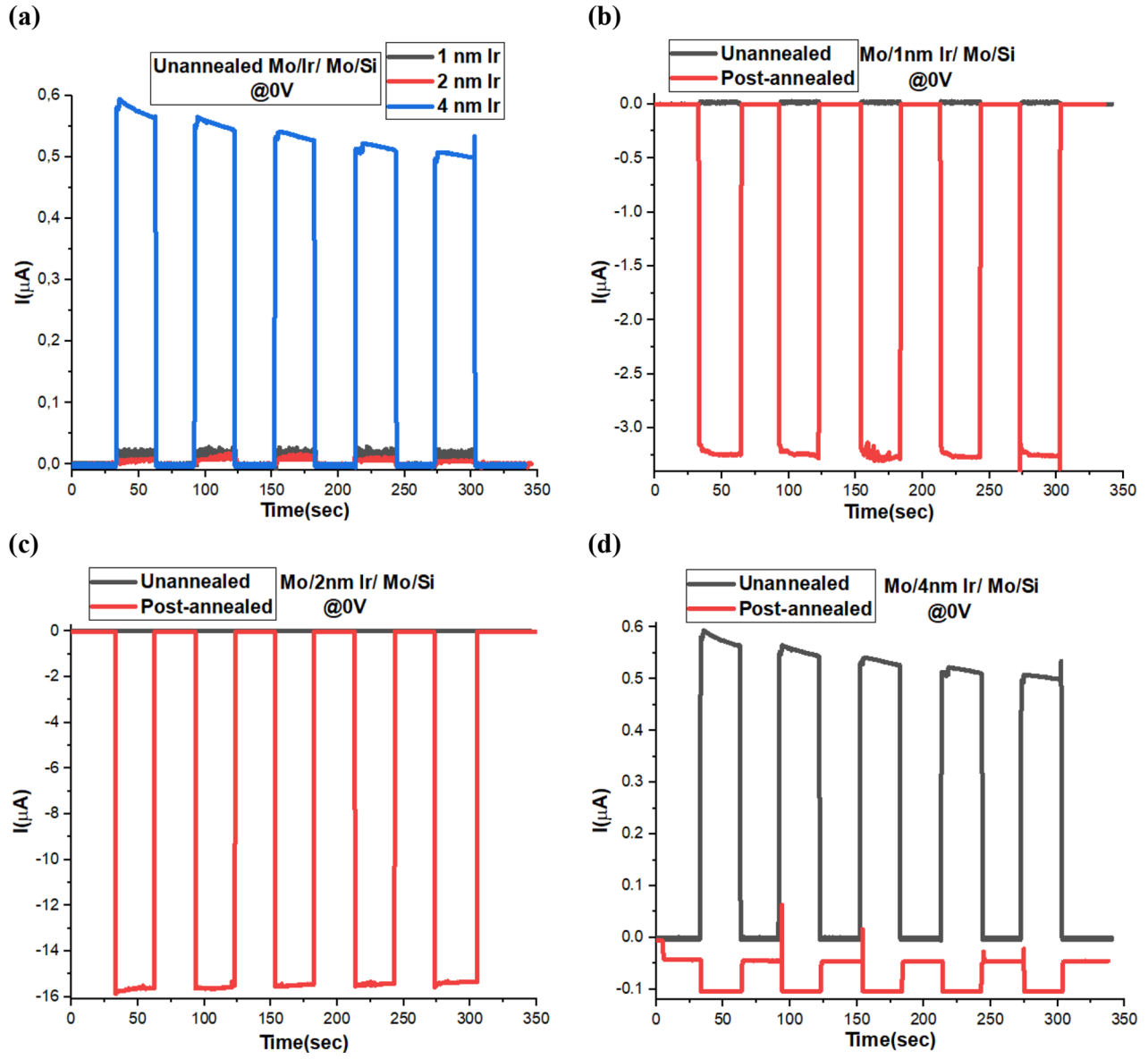

Figure 4. Illustrates the self-powered OFF-ON response of unannealed MoO_3/Ir/MoO_3/Si samples with varying Ir layer thicknesses: 1, 2, and 4 nm (a). Additionally, the behavior of MoO_3/Ir/MoO_3/Si samples for both unannealed and post-annealed conditions is shown for the 1 nm Ir layer (b), 2 nm Ir layer (c), and 4 nm Ir layer (d), all under zero voltage bias.

indicated that the introduction of light triggered a distinct shift in the current behavior near the origin point. This transformation likely stems from the interaction between the incident light and the inherent properties of the material, leading to adjustments in the electrically conductive attributes of the samples.

Due to the significant difference in intensity between the levels of dark and ultraviolet (UV) illumination, we decided to improve the representation of the data. To achieve this, separate plots for each illumination condition are created, as illustrated in Figure 3d−g. Upon analysis of these plots, a noticeable observation is that the unannealed samples, under both dark and illuminated conditions, exhibit behavior that deviates from what is known as Ohmic behavior. This outcome was somewhat anticipated due to the quality of MoO_3 present on the surface. The rectification was found to be highest for the MoO_3/4 nm Ir/MoO_3/Si sample, generating a photocurrent of 20,000 μA at 10 V followed by the MoO_3/2 nm Ir/MoO_3/Si sample, which generated a photocurrent of 10,000 μA at 10 V. The MoO_3/1 nm Ir/MoO_3/Si sample showed the lowest generated photocurrent of 2000 μA at 10 V. It is important to note that the $I-V$ curves were found to be free from noise and disturbances under all measurements. Furthermore, a comparison between the unannealed and postannealed samples for the MoO_3/Ir/MoO_3/Si group revealed that the post-annealed samples exhibited enhanced photocurrent. This material's crystalline structure is not highly developed, leading to the formation of what is referred to as Schottky behavior when in contact with Ag contacts. However, after subjecting the samples to an annealing process, significant improvements. This annealing process directly enhances the grain structure on the surface and promotes the growth of higher-quality crystals. Consequently, this refinement of the material's structure leads to a transformation in its behavior. Specifically, the transport properties are enhanced and the overall conductivity of the final device is increased. This suggests that the annealing process plays a

https://doi.org/10.1021/acsaelm.3c01047
ACS Appl. Electron. Mater. 2023, 5, 5696−5713

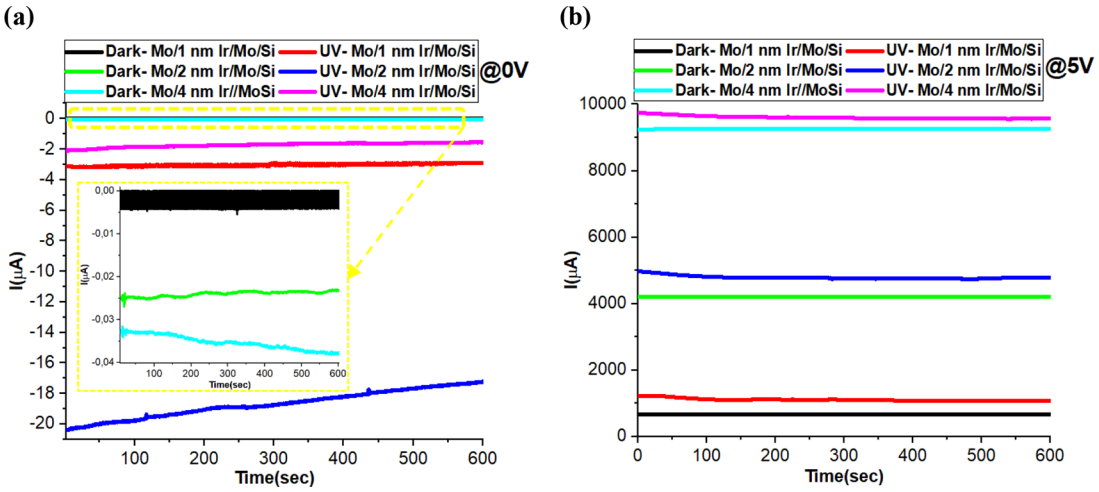

Figure 5. Temporal stability of MoO_3/Ir/MoO_3/Si PDs under dark and UV illuminations with varying 1, 2, and 4 nm Ir thickness and a bias voltage of 0 (a) and 5 V (b).

crucial role in optimizing the performance of the device by improving the material's properties, resulting in improved electrical conductivity.

UV Photodetector Performances. The study explores how the presence of different thicknesses of the Ir layer (1, 2, and 4 nm) affects the OFF-ON behavior of the thin film structure. The OFF-ON behavior refers to how well the thin film structure responds under dark and UV illuminations at 0 V for both groups of unannealed and post-annealed MoO_3/Ir/MoO_3/Si, as shown in Figure 4.

In Figure 4a, it can be seen that the positive photoresponses of the unannealed samples are limited to 0.6 μA under UV illumination at a 0 V bias. The 4 nm Ir sample exhibits the highest photocurrent, while the 1 and 2 nm Ir samples have the lowest with a small difference of less than 0.05 μA. Moreover, these curves exhibit excellent response dynamics during OFF-ON conditions. To investigate the impact of annealing on photoresponses, we compared the unannealed and postannealed samples in each group of 1, 2, and 4 nm Ir layers as in Figure 4b–d. In the case of 1 nm Ir, we observed a significantly higher negative photocurrent in the postannealed samples, reaching 3.5 μA, whereas the unannealed samples exhibited only a small photocurrent. Similarly, for the 2 nm Ir samples, the negative photocurrent in the postannealed samples increased to 16 μA. On the other hand, the 4 nm Ir sample showed a negative photocurrent of only 0.1 μA and poor dynamic behavior compared to the 1 and 2 nm samples. Interestingly, the 2 nm Ir sample showed the highest photocurrent under negative photocurrent behavior, while the 4 nm Ir sample exhibited the lowest. Overall, we observed an inverse relationship between the positive and negative photocurrent behaviors of the unannealed and postannealed samples, with higher negative photocurrents. These results show that 1 and 2 nm Ir are more interesting for enhanced plasmonic effects.

In addition, for checking the performance under higher voltages (0.5–5 V) and comparing it with 0 V performances, Figure S1 (Supporting Information) depicts the performance characteristics of unannealed and post-annealed MoO_3/Ir/MoO_3/Si devices with varying thicknesses of 1, 2, and 4 nm for the Ir layers under different applied bias voltages ranging from 0 to 5 V. The results show that despite the differences between the unannealed and post-annealed samples, both groups demonstrate well-defined OFF-ON responses with fast response and recovery behaviors. This suggests that regardless of the annealing condition, the devices exhibit reliable and efficient switching characteristics. These results are inconsistent with diffuse reflectance (R) measurements as in Figure S3 (Supporting Information). R reveals an absorption peak around 365 nm, which slightly shifts toward longer wavelengths with increasing thickness.

Temporal Stability under 0 V. The performance of PDs cannot be solely determined from the I–V curves recorded at higher voltages. To obtain a better understanding of their capabilities, this study aimed to investigate the temporal stability of a specific type of PD composed of MoO_3/Ir/MoO_3/Si layers with varying thicknesses of Ir (1, 2, and 4 nm) under 0 V bias. The PD was subjected to both darkness and UV light and powered with 0 and 5 V, as in Figure 5, to evaluate its stability over time. The results of this study have the potential to enhance our comprehension of designing and utilizing PDs in fields such as optoelectronics and photonics. The PDs' temporal stability was analyzed by measuring their response to UV light and darkness over a period. At 0 V bias, all samples of the PD exhibited negative photoresponses, which were stable for a long time. The sample with a 2 nm thick Ir layer demonstrated the highest photocurrent of 20 μA, followed by the 1 nm Ir layer, which exhibited a photocurrent of 3 μA. In contrast, the sample with a 4 nm Ir layer showed a very low photocurrent of 2 μA. These findings suggest that thinner films of 1 and 2 nm Ir layers can potentially excite more hot electrons than thicker films of 4 nm, which may have implications in the development of more sensitive and efficient PDs for optoelectronics and photonics applications. These results confirm that ultrathin films of 1 and 2 nm Ir layers have the potential to excite more hot electrons than thicker films of 4 nm. This phenomenon could be attributed to the fact that thinner layers require less energy to generate hot electrons, which could contribute to the higher photocurrent observed in the samples with thinner Ir layers.

For the 5 V bias condition, it is apparent that the photocurrent increases as the Ir thickness increases. This suggests that a higher Ir content leads to a stronger response to UV illumination, resulting in a greater photocurrent. Therefore, the device's sensitivity to UV light improves with an increase in the thickness of the Ir layer. Additionally, the dark current of the photodetector varies with the Ir content. Among the samples, one with a 4 nm Ir layer exhibits the highest dark current value. This

https://doi.org/10.1021/acsaelm.3c01047
ACS Appl. Electron. Mater. 2023, 5, 5696–5713

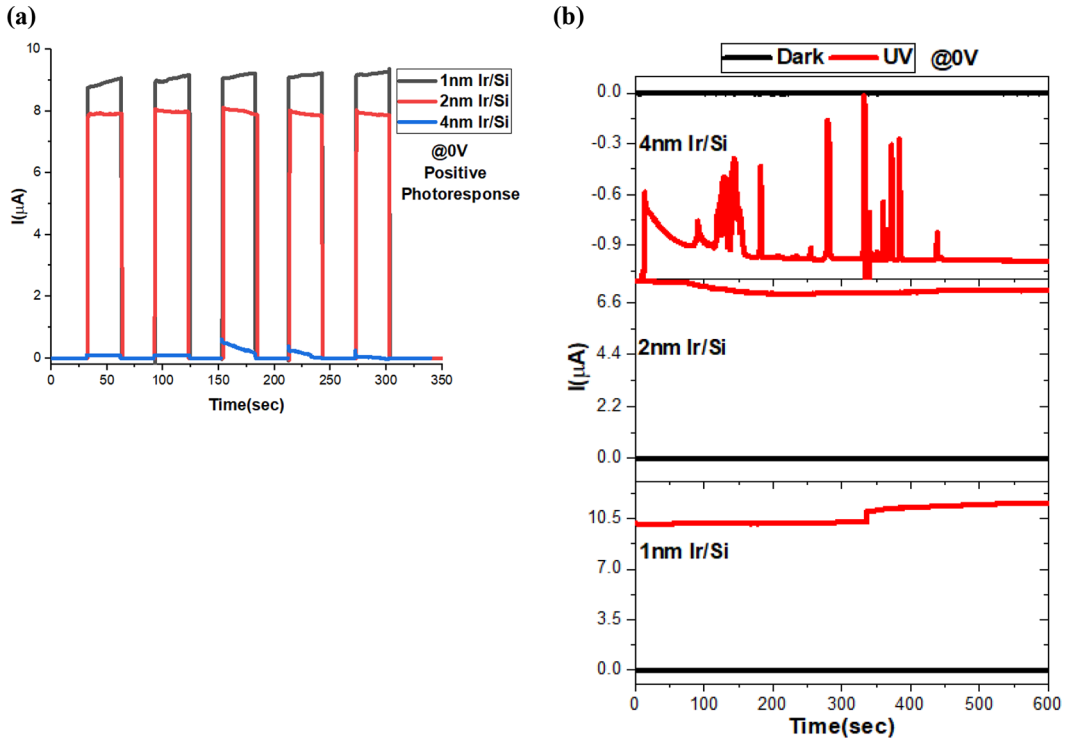

Figure 6. OFF-ON photoresponse (a) and transient response behavior under dark and UV illuminations (b) at 0 V of Ir/Si sample with different thicknesses of the Ir layer of 1, 2, and 4 nm.

implies that a thicker Ir layer contributes to a higher level of the dark current in the device. It is important to note that the dark current represents the current flowing through the device in the absence of any light stimulus, and a higher dark current can impact the overall performance and signal-to-noise ratio of the photodetector. Therefore, the findings suggest that thinner Ir layers could enhance the performance of PDs by improving their sensitivity and efficiency, which could have significant implications for various applications in optoelectronics and photonics.

Further investigations were conducted on the optoelectronic performance of Ir/ Si structures with varying thicknesses of 1, 2, and 4 nm to gain a comprehensive understanding of the role of the Ir layer in the absence of MoO_3 layers. Figure 6 presents the results obtained from these investigations, shedding light on the underlying mechanisms behind the observed phenomena, such as the significantly reduced plasmonic behavior exhibited by the 4 nm Ir layer and the origin of the negative photocurrents observed in the MoO_3/Ir/MoO_3/Si structures after the post-annealing process. Upon initial examination of the OFF-ON behaviors depicted in Figure 6a, it becomes apparent that the 1 and 2 nm Ir thickness conditions yield the highest photocurrents, exhibiting only minor differences with respect to each other under UV illuminations. Conversely, the 4 nm Ir thickness condition demonstrates the lowest photocurrent, displaying irregular patterns. It is important to note that the efficiency of hot carrier generation relies on various factors, including the thickness of the plasmonic layer. Generally, thinner plasmonic layers tend to generate a greater number of hot carriers compared to thicker layers, as elucidated elsewhere.[46] This can be attributed to the more efficient decay of surface plasmons in thinner layers, leading to a higher probability of hot carrier generation.

Furthermore, an interesting observation can be made regarding the behavior of the nanometer Ir layer over time, particularly it is very low photocurrents, as depicted in Figure 6b. This observation further reinforces the notion that the integration of the nm Ir layer is unsatisfactory for optoelectronic devices based on Ir. However, it is worth noting that both the 1 and 2 nm Ir layers exhibit comparable dark currents and demonstrate more stable photocurrents. These results corroborate the previous findings indicating that the 1 and 2 nm Ir layers yield the highest photoresponses, while the 4 nm Ir layer exhibits significantly lower photoresponses. Additionally, the Hall effect measurements of the Ir/Si device of 1, 2, and 4 nm thickness are depicted in Table S1 (Supporting Information). The results suggest that there is a higher density of charge carriers of 2.07×10^{20} cm^{-3} present in the 1 nm Ir layer compared to the others, 6.45×10^{19} and 5.48×10^{17} cm^{-3} for the 2 and 4 nm Ir layer, respectively. Of particular interest is the fact that these photoresponses, for all three thicknesses of Ir layers (1, 2, and 4 nm), are positive. This observation suggests that the Ir layer, regardless of its thickness, is not responsible for the negative photoresponses observed in the MoO_3/Ir/MoO_3/Si structures. Instead, this strongly implies that the MoO_3 sandwich layers play a critical role in generating negative photoresponses. However, the case of postannealed 4 nm Ir/Si shows nonstability through time. This effect is similar to some reported studies, including the NPC phenomenon that was observed by Fu-Cheng Wang and colleagues in single quantum wells of InAs/AlSb that can be electrically resettable.[47] This is caused by the capture of photoexcited electrons through deep levels in AlSb, resulting in a decrease in the carrier density. A similar mechanism was also reported by Sadofyev et al. for NPC in the same system.[48]

Hall Effect and Carrier Concentrations. The Hall effect measurements were performed at room temperature, and the

https://doi.org/10.1021/acsaelm.3c01047
ACS Appl. Electron. Mater. 2023, 5, 5696−5713

Table 1. Surface Sheet Resistance (R_s), Resistivity (R_{ho}), Hall Voltage (V_H), Hall Coefficient (R_H), Sheet Carrier Concentration (N_s/P_s), Carrier Concentration (N/P), and Mobility (Mob) for Both Unannealed and Post-annealed Samples

code	sample	R_s (ohm/sq)	R_{ho} (/ohm cm)	V_H(V)	R_H(m^3/C)	type	N_s/P_s (/cm^2)	N (/cm^3)	mobility (cm^2/(V s))
unannealed	MoO_3/1 nm Ir/MoO_3/Si	1.68×10^6	1.06×10^0	-6.98×10^{-3}	-6.13×10^{-5}	n	-6.45×10^{10}	-1.02×10^{17}	5.76×10^1
	MoO_3/2 nm Ir/MoO_3/Si	5.25×10^5	3.80×10^{-1}	-7.75×10^{-3}	-2.59×10^{-4}	n	-1.74×10^{10}	-2.41×10^{16}	6.83×10^2
	MoO_3/4 nm Ir/MoO_3/Si	5.66×10^4	5.31×10^{-2}	-1.45×10^{-2}	-3.77×10^{-5}	n	-1.55×10^{11}	-1.66×10^{17}	7.09×10^2
post-annealed	MoO_3/1 nm Ir/MoO_3/Si	3.02×10^4	3.42×10^{-2}	-1.32×10^{-5}	-6.92×10^{-7}	n	-1.02×10^{13}	-9.02×10^{18}	2.02×10^1
	MoO_3/2 nm Ir/MoO_3/Si	2.11×10^5	2.58×10^{-1}	2.41×10^{-5}	4.09×10^{-7}	p	1.87×10^{13}	1.52×10^{19}	1.58×10^0
	MoO_3/4 nm Ir/MoO_3/Si	1.67×10^4	2.40×10^{-2}	-1.08×10^{-4}	-2.16×10^{-6}	n	-4.15×10^{12}	-2.89×10^{18}	8.99×10^1

recorded data are listed in Table 1. It was observed that the carrier concentrations directly correlated with the results obtained from the $I-V$ measurements. Additionally, due to its highly conductive metallic nature, it was expected that Ir would exhibit significant carrier concentrations. On the other hand, the mobility of the carriers indicates how quickly electrons or holes move through the sample, specifically from the sample to the contacts. Essentially, the mobility factor reflects the sensitivity, detectability, and response characteristics (ON/OFF) of the samples, as reflected in the results. Another interesting observation is that thicker layers of Ir resulted in higher carrier concentrations, which can be attributed to the plasmonic properties of Ir as a metal, enabling the direct introduction of high carrier concentrations. In addition, it is known that plasmonic materials can induce more carrier concentrations (plasma frequencies) and faster carrier mobilities (plasmon damping constants).[49,50]

Also, all samples present an n-type semiconducting behavior except for the post-annealed MoO_3/2 nm Ir/MoO_3/Si sample. It is noted that by passing the post-annealing process, carrier concentration (N/P) is enhanced due to the large enhancement in the film crystallinity and acquiring oxygen vacancies, which act as electron donor centers. However, the mobility seems not to be so high, and it is a bit inversely proportional to the N concentrations. In simple terms, when there are high carrier concentrations, this suggests that there is a large number of charge carriers available for transportation. However, because there are so many carriers nearby, they tend to interact with each other or with impurities and defects in the material. These interactions can cause the carriers to scatter or collide with defects (e.g., oxygen vacancies), making it harder for them to move freely. MoO_3 has been identified as a material with a significant number of oxygen vacancies.[51,52] These vacancies could interact with the charge carriers present in the material, resulting in higher concentrations. When a large number of vacancies are involved, the higher carrier concentrations may hinder the smooth flow and ultimately reduce their mobility. In simpler terms, the interactions between the vacancies and carriers impede the carriers' ability to move freely, leading to lower mobility, as represented in Figure 7.

Negative Photoconductivity in MoO_3/Ir/MoO_3. The occurrence of both PPC and NPC has been observed in numerous materials and is influenced by several factors including light wavelength, intensity, applied bias voltage, relative humidity, temperature, and composition. The coexistence of PPC and NPC is not a universal phenomenon and varies depending on the specific conditions under which the material is tested. For instance, in WO_3 nanowires,[15] hybrid perovskite semiconductors,[18] a mix of cubic zinc-blend and hexagonal wurtzite phases in III–V semiconductor nanowires,[53] p-type Pb1-xSnxTe film,[25] single-layer graphene (SLG)-carbon nanotube thin film (CNTF) Schottky junction,[54] Pb/Sn perovskite,[55] $CsPbX_3$ (X = Cl, Br, or I) nanoheterojunctions,[56] bidoped hybrid halide perovskites octahedral semiconductors,[57] $CsPbBr_3$/graphene heterojunction,[58] $Zn_{1-x}Cd_xO$ films,[27] graphene,[59] and 2D $FePS_3$.[60] In our case, the bias voltage well contributed to the positive and negative photocurrent. Several factors can contribute to the release of negative photoconductivity under light illumination, as previously mentioned. First, the photoresponse of only MoO_3/Si has been checked for understanding the role of the oxide layer. Figure 8 illustrates the MoO_3/Si OFF-ON photoresponses under UV illumination, providing valuable insights into the underlying factors responsible for the negative photoconductivity in MoO_3/Ir/MoO_3/Si. Notably, the deposition conditions for the MoO_3 layer closely resemble those of the MoO_3layer in the MoO_3/Ir/MoO_3/Si structure. Additionally, both the MoO_3 layer in MoO_3/Ir/MoO_3/Si and the MoO_3/Si undergo postannealing processes, ensuring comparable conditions for deposition. Thus,

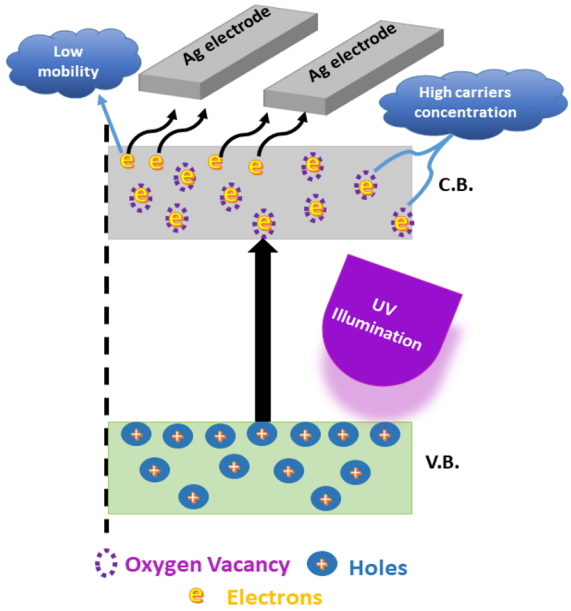

Figure 7. Schematic band gap diagram of the possible mechanism of carrier concentrations and the mobility as predicted from Hall effect measurements.

https://doi.org/10.1021/acsaelm.3c01047
ACS Appl. Electron. Mater. 2023, 5, 5696–5713

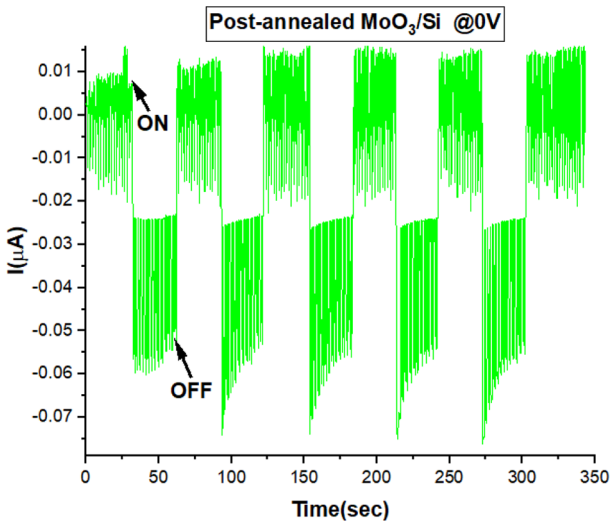

Figure 8. OFF-ON photoresponse of post-annealed MoO_3/Si under 0 V bias. It shows a negative photoresponse.

we can confidently assert that the MoO_3/Si and MoO_3/Ir/MoO_3/Si structures share the same deposition conditions. Through a thorough examination of the MoO_3/Si behavior, it is evident that it exhibits a negative photoresponse.

O_2 Adsorption/Desorption Mechanism. , as shown in eqs 1−4.

$$O_2(gas) \rightarrow O_2(ads) \quad (1)$$

$$O_2(gas) + e^- \rightarrow O^-_2(ads) \quad (\text{low temperature; } T < 100^\circ C) \quad (2)$$

$$O^-_2(ads) + e^- \rightarrow 2O^-(ads) \quad (\text{intermediatetemperature; } 100 < T < 300^\circ C) \quad (3)$$

$$O^-(ads) + e^- \rightarrow O^{2-}(ads) \quad (\text{highertemperature; } T > 300^\circ C) \quad (4)$$

The fact behind this is coming from the post-annealing process in an air environment at a bit high temperature. For the postannealed samples, under UV light irradiation, the MoO_3 ultrathin films undergo a process where some of the adsorbed O_2 molecules from the environment are desorbed from their surface.[61] This releases electrons back to MoO_3, leading to an increase in its carrier density. As a result, the equilibrium between the Fermi levels of the MoO_3 and Ir layer is disrupted.[62] Some of the released electrons move to the Ir layer and recombine with the holes in it, while some behave as Coulomb traps at the MoO_3/Ir interface. The latter quenches the holes of the Ir layer and lowers the hole mobility, which reduces the transport in the Ir layer. While the desorption of O_2 molecules from the surface of MoO_3 can contribute to an increase in the carrier density of MoO_3, not all of the liberated electrons are injected into the Ir layer or function as Coulomb traps. The increase in carrier density does enhance the transport properties of MoO_3 up to a certain threshold. However, due to the high carrier mobility of the Ir layer, the change in transport predominantly stems from the Ir layer rather than the entire heterostructure. Consequently, under light irradiation, the resistance of the heterostructure increases, resulting in a decrease in current. Additionally, in the absence of a post-annealing process, nearly all adsorbed O_2 molecules desorb, which accounts for the significantly higher resistance observed in the unannealed heterostructure compared to the post-annealed samples. Similar behavior has been reported in the previous

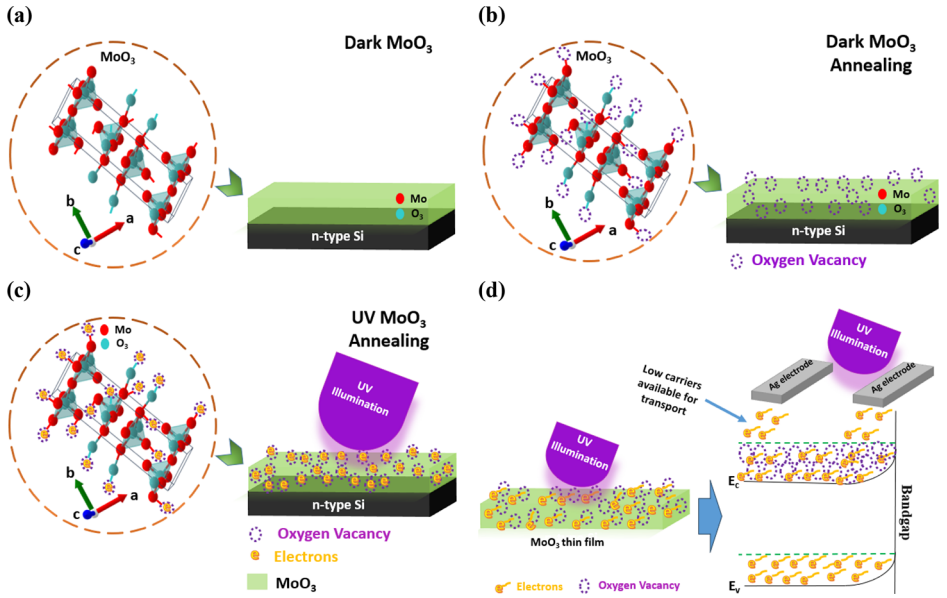

Figure 9. Schematic diagram depicting the potential process involved in the creation of oxygen vacancies responsible for the negative detector behavior on the surface of MoO_3. In the initial state, a nonannealed MoO_3 thin film is shown (a). Upon undergoing a post-annealing procedure in an air environment, the annealing process induces the formation of oxygen vacancies (b). Subsequently, upon exposure to light, the generated electrons occupy these oxygen vacancies, leading to an increase in carrier concentrations. However, this also results in a constraint on mobility (c). Consequently, the limited carrier mobility causes a reduced transfer to the metal contacts (d).

https://doi.org/10.1021/acsaelm.3c01047
ACS Appl. Electron. Mater. 2023, 5, 5696−5713

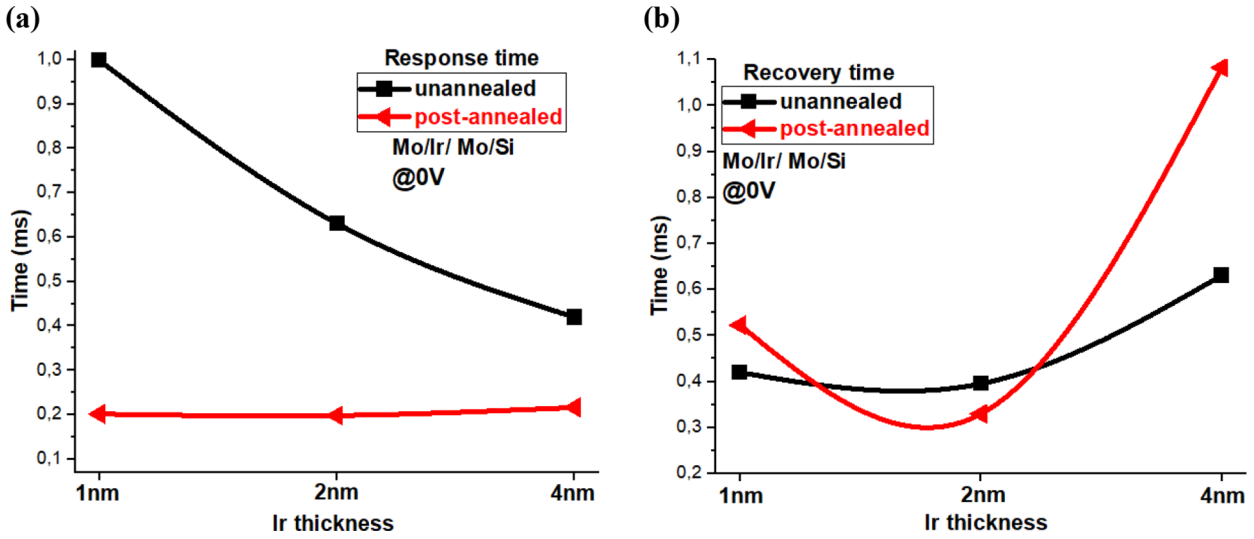

Figure 10. Response time (a) and recovery time (b) at 0 V voltage of unannealed and postannealed MoO_3/Ir/MoO_3/Si with different thicknesses of the Ir layer of 1, 2, and 4 nm.

literature.[24,63] The generated photocurrent in our case is higher than that reported in MoO_3/graphene structures,[24] TiO_2-decorated graphene,[61] and $FePS_3$ UV PD.[60]

In contrast to the behavior observed under light irradiation, the absence of light resulted in the adsorption of some O_2 molecules onto the material's surface. These adsorbed molecules acted as traps for the electrons in MoO_3, forming anions and reducing the overall electron population in MoO_3. Consequently, the Fermi level of the material decreased. To maintain alignment between the Fermi level of MoO_3 and the Ir layer, the Fermi level of Ir also shifted downward. This shift caused an increase in the number of hole carriers within the Ir layer. Moreover, the decrease in the number of electrons in MoO_3 led to a reduction in the number of charge traps, resulting in an enhancement of the hole mobility within the Ir layer. As a result, the current passing through the sample increased in the absence of light. However, it was observed that the recovery of the current was slower than the initial decrease, indicating that the adsorption of oxygen molecules was a more challenging process compared to desorption.

In summary, under UV light irradiation, desorption of the ligand of the O_2 molecules from the MoO_3 surface releases electrons, which increases its carrier density. This led to decreased transport in the Ir layer due to Coulomb trapping and lowered hole mobility. While the carrier density in MoO_3 may increase, leading to potential enhancements in transport, the change in transport primarily depends on the behavior of the Ir layer within the heterostructure. Consequently, the decrease in transport observed in the Ir layer outweighs any potential increase in the level of MoO_3 transport. As a result, under light irradiation, the resistance of the heterostructure increases, ultimately leading to a decrease in the current flowing through the system.

Effect of Oxygen Vacancy. Nonetheless, the functioning of the MoO_3 device is impacted by elevated levels of bulk defects,[64−67] leading to instabilities in the flat-band voltage. The presence of these defects becomes evident through several experimental methods, such as trap-assisted electron conduction involving the Poole−Frenkel mechanism,[68−70] direct electron injection,[71] and optical absorption.[72] Although the specific energy levels of the defects vary across different experiments, the oxygen vacancy is typically identified as their shared physical source.[72−74] By this means, an oxygen vacancy has become interesting with direct contributions to optoelectronic conductivity.[75] A schematic diagram explaining the role of the oxygen vacancy in this MoO_3 structure is presented in Figure 9. The behavior of electrons is studied when they transition from the valence band to a defect level situated within the band gap of the material. This transition occurs when an electron absorbs a photon and gains enough energy to move from the lower energy valence band to the higher energy defect level. In the absence of light (Figure 9a), the MoO_3 sample exhibited distinct and well-defined crystal structures. However, upon subjecting the MoO_3 film to an annealing process in an air environment, an interesting phenomenon occurred. The MoO_3 film began to exhibit an increased presence of oxygen vacancies, as illustrated in Figure 9b. These oxygen vacancies arise due to the formation or desorption of lattice oxygen atoms,[76] resulting in the creation of trap states within the material. Then, when the MoO_3 sample is exposed to light, specifically under light illumination conditions, a notable transformation takes place; electrons in the valence band gain sufficient energy from the incident light and transition to the conduction band. As depicted in Figure 9c, these free electrons subsequently become captured by the existing oxygen vacancies within the material, which directly decrease the carrier mobility and increase the carrier concentrations to a large amount and consequently inverse the conductivity. The oxygen vacancies, acting as trapping sites, effectively capture and immobilize the free electrons, resulting in modified electronic behavior and the response of the MoO_3 film under illumination. These results confirm the Hall effect findings (Table 1) of presenting oxygen vacancy trap states and consequently produce the negative conductivity behavior of the PDs.

Response and Recovery Time. It is crucial to investigate how quickly the material can detect UV light without a bias voltage to gain a better understanding of the optoelectronic behavior of the ultrathin Ir layer during the annealing and post-annealing process. Upon ceasing UV light exposure, the signal starts to decay until it reaches the lowest dark current level, which indicates the recovery time. Figure 10 shows the measurements of the response and recovery time for the unannealed and post-annealed MoO_3/Ir/MoO_3/Si samples.

https://doi.org/10.1021/acsaelm.3c01047
ACS Appl. Electron. Mater. 2023, 5, 5696−5713

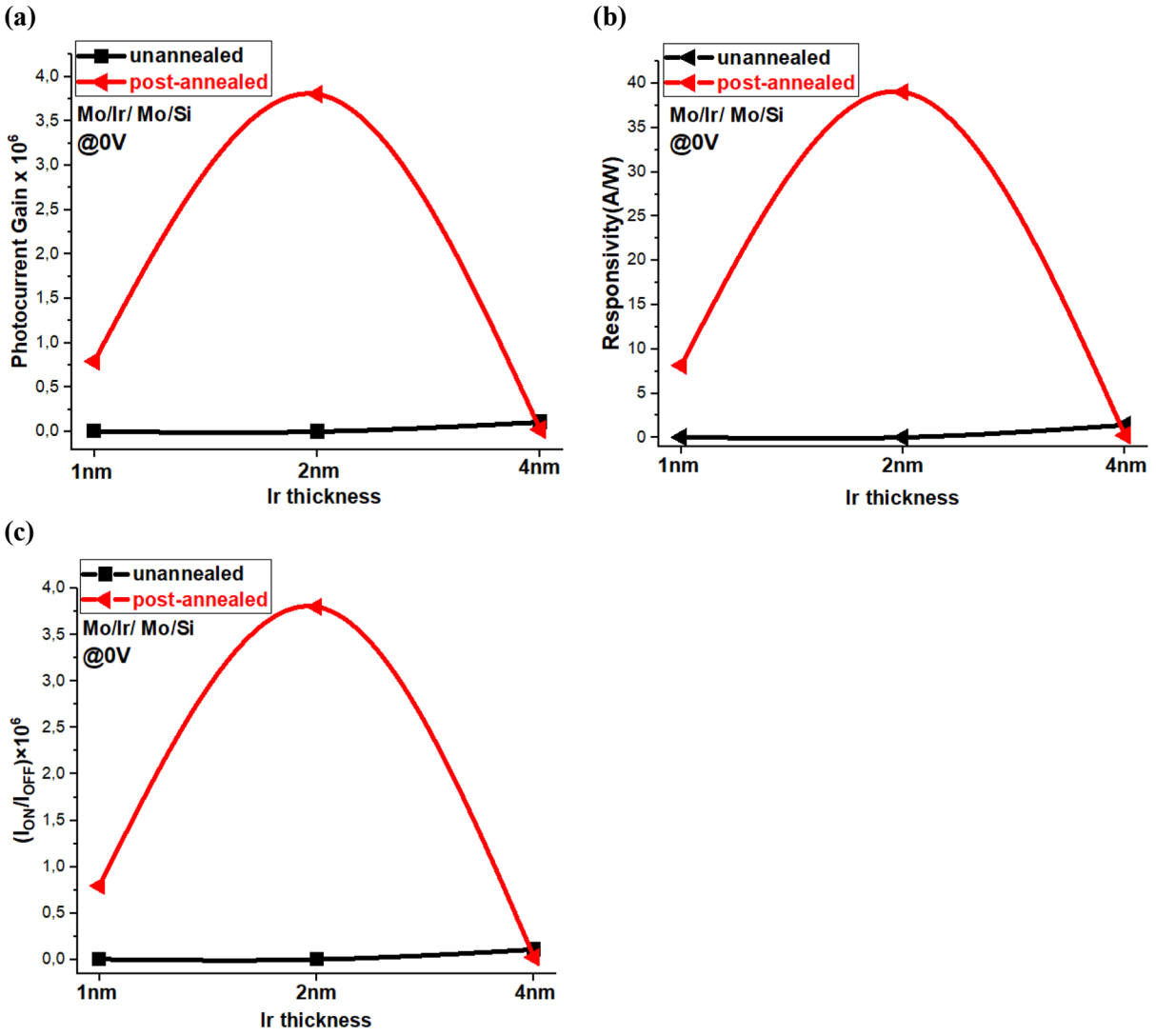

Figure 11. Photocurrent gain (a), responsivity (b), and the I_{ON}/I_{OFF} ratio (c) at 0 V of unannealed and post-annealed MoO_3/Ir/MoO_3/Si of different thicknesses of the Ir layer of 1, 2, and 4 nm.

Notably, all samples exhibit faster response times than recovery times. The post-annealed samples display a faster response time compared to the unannealed samples. This behavior can be attributed to the annealing process, which improves the crystallinity of the film and enhances the fast electron transfer process. The response time of the postannealed samples is approximately 0.2 ms for the 2 nm Ir sample, with a slight increase toward the 1 and 4 nm Ir layer. In contrast, the response time for the unannealed samples reached 1 ms. Furthermore, the recovery time of the postannealed samples reaches its lowest value at the 2 nm Ir layer, measuring 0.33 ms. In contrast, the unannealed samples require a slightly longer time of 0.41 ms for the 2 nm Ir sample to recover. This observation may be due to the postannealing process's ability to enhance the material's crystallinity, which helps facilitate carrier transport, thus reducing the recovery time.

The plasmonics of the Ir layer play a crucial role in enhancing the performance of the UV PD. When the Ir layer is exposed to UV light, it generates excited electrons that are transferred to the metal layer's surface, leading to the excitation of plasmons. Plasmons are collective oscillations of free electrons in a metal that generate an enhanced electromagnetic field around the metal surface. This increased field creates a higher local density of optical states, which can enhance the absorption of the UV light. The increased absorption of UV light due to plasmonics leads to a significant increase in the photocurrent generated by the PD. The increased photocurrent results in a faster response time, as more carriers are generated and transferred through the device. This enhanced response time is particularly important in applications where the rapid detection of UV light is required. Moreover, plasmons can also assist in reducing the recovery time of PD. After the UV light is removed, the excited holes relax, which is a slow process that limits the PD's response speed. However, the plasmons can accelerate the carrier mobility process by enhancing the local density of states around the metal surface and thus reducing the recovery time of the PD.

Overall, these findings indicate that post-annealing the ultrathin Ir layer can significantly improve the material's optoelectronic properties, resulting in faster response and recovery times. Additionally, the results suggest that the thickness of the Ir layer plays a role in determining the material's response and recovery times, whereas a thinner layer has a faster response and recovery time. By this means, the plasmonics of the Ir layer can significantly enhance the performance of the UV PD

https://doi.org/10.1021/acsaelm.3c01047
ACS Appl. Electron. Mater. 2023, 5, 5696−5713

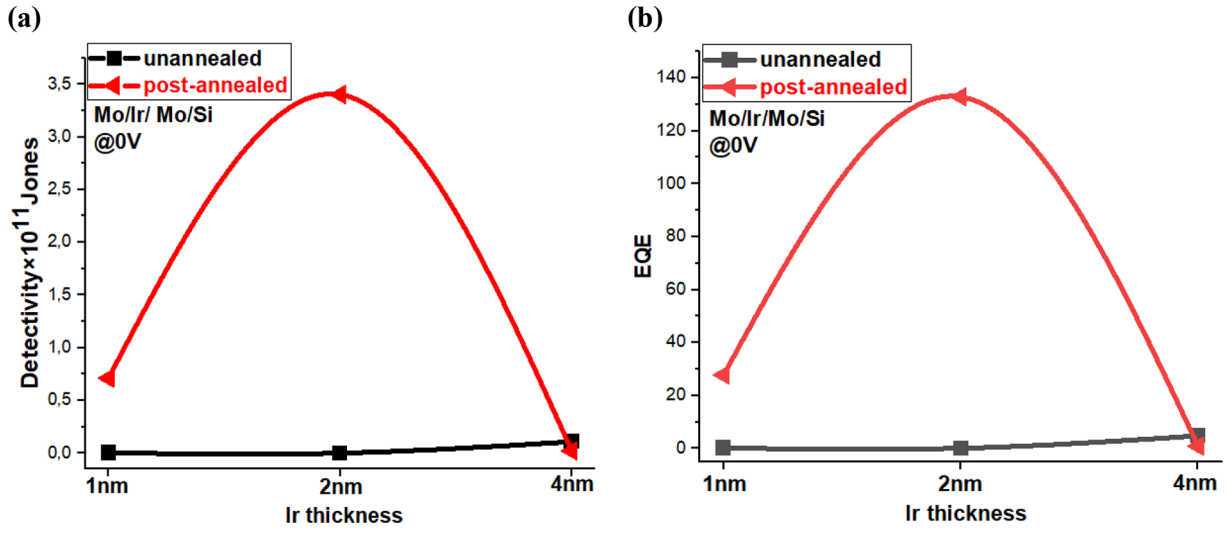

Figure 12. Detectivity (a) and EQE (b) at 0 V of unannealed and post-annealed MoO_3/Ir/MoO_3/Si with different thicknesses of the Ir layer of 1, 2, and 4 nm.

by increasing the absorption of UV light and increasing the carrier concentrations. The improved response and recovery times achieved through plasmonics can make the UV PD more suitable for applications requiring the rapid and sensitive detection of UV light.

Photocurrent Gain and Responsitivity. Figure 11 presents a detailed analysis of the optoelectronic properties of MoO_3/Ir/MoO_3/Si structures with varying thicknesses of the Ir layer (1, 2, and 4 nm). The figure provides information on the photocurrent gain, responsivity, and the I_{ON}/I_{OFF} ratio at 0 V for both unannealed and post-annealed samples. In Figure 11a, the photocurrent gain for each Ir layer thickness is shown. It is observed that the 1 and 2 nm Ir layers exhibit higher photocurrent gains compared to the 4 nm Ir layer, especially undergoing the post-annealing process, indicating their superior ability to generate photocurrents in response to external illumination. The post-annealed MoO_3/2 nm Ir/MoO_3/Si sample demonstrates the highest value among the tested samples, reaching 3.8E6, when evaluated as a self-powered PD. This result indicates that the MoO_3/2 nm Ir/MoO_3/Si structure, after undergoing the post-annealing process, exhibits remarkable performance in converting incident light into electrical signals without requiring an external power source. The high value of 3.8E6 signifies a significantly amplified photocurrent response to incident light. This suggests that the MoO_3/2 nm Ir/MoO_3/Si sample efficiently captures photons and converts them into electrical currents, making it an excellent candidate for self-powered PD applications.

Figure 11b displays the responsivity at 0 V of the MoO_3/Ir/MoO_3/Si structures with different Ir layer thicknesses. Figure S6 (Supporting Information) shows the responsivity as a function of voltages of 0, 0.5, 1, 2, 3, 4, and 5 V for unannealed and post-annealed MoO_3/Ir/MoO_3/Si thin films at a UV 365 nm wavelength light source. The responsivity values reflect how efficiently the devices convert incident light into electrical signals. The results indicate that the 2 nm Ir layer exhibits a higher responsivity of 39 A/W compared to both the 1 and 4 nm Ir layers. This suggests that the 2 nm Ir layer is more sensitive to light and produces stronger electrical responses when subjected to a 0 V bias under the post-annealing process. The observed behavior aligns with the trend observed in the photocurrent gain, further supporting the notion that the thickness of the Ir layer influences the device's light sensitivity and electrical response. The higher responsivity of the 2 nm Ir layer indicates its ability to more efficiently convert incident light into electrical signals, making it a favorable choice for optoelectronic applications requiring enhanced light detection capabilities. In Figure 11c, the I_{ON}/I_{OFF} ratio at 0 V is presented, which measures the device's ability to switch between the ON and OFF states. A higher I_{ON}/I_{OFF} ratio indicates a more distinct differentiation between these states. The data reveal that the 2 nm Ir layer exhibits a higher. I_{ON}/I_{OFF} ratios of 3.8×10^6 compared to both the 1 and 4 nm Ir layers. This indicates that the 2 nm Ir layer possesses superior switching capabilities compared with the other two thicknesses. The higher I_{ON}/I_{OFF} ratio of 3.8×10^6 for the 2 nm Ir layer signifies a more pronounced distinction between the ON and OFF states of the device. Importantly, the achieved. I_{ON}/I_{OFF} ratio of 3.8×10^6 for the 2 nm Ir layer surpasses values reported in existing literature reviews. This highlights the notable performance of the 2 nm Ir layer in terms of its switching characteristics, demonstrating its potential for advancement in optoelectronic devices and surpassing previously reported results. The observed improvements in photocurrent gain, responsivity, and I_{ON}/I_{OFF} ratio in the postannealed samples of the MoO_3/Ir/MoO_3/Si structures can be attributed to several factors. The postannealing process enhances the crystalline structure, reducing defects and improving charge transport properties. It also promotes better interface formation between the layers, enhancing the efficiency of charge transfer and increasing responsivity. Additionally, post-annealing optimizes the doping and carrier concentration profiles, reducing leakage current and improving the I_{ON}/I_{OFF} ratio.

Detectivity and EQE. In Figure 12, the detectivity and EQE at 0 V are presented for both unannealed and postannealed MoO_3/Ir/MoO_3/Si samples with varying thicknesses of the Ir layer (1, 2, and 4 nm). The detectivity measurement provides valuable insights into the sensitivity and noise performance of the PDs, while the EQE measurement indicates the efficiency of converting incident photons into electrical currents. These measurements play a pivotal role in optimizing device design, material selection, and fabrication processes to enhance

https://doi.org/10.1021/acsaelm.3c01047
ACS Appl. Electron. Mater. 2023, 5, 5696−5713

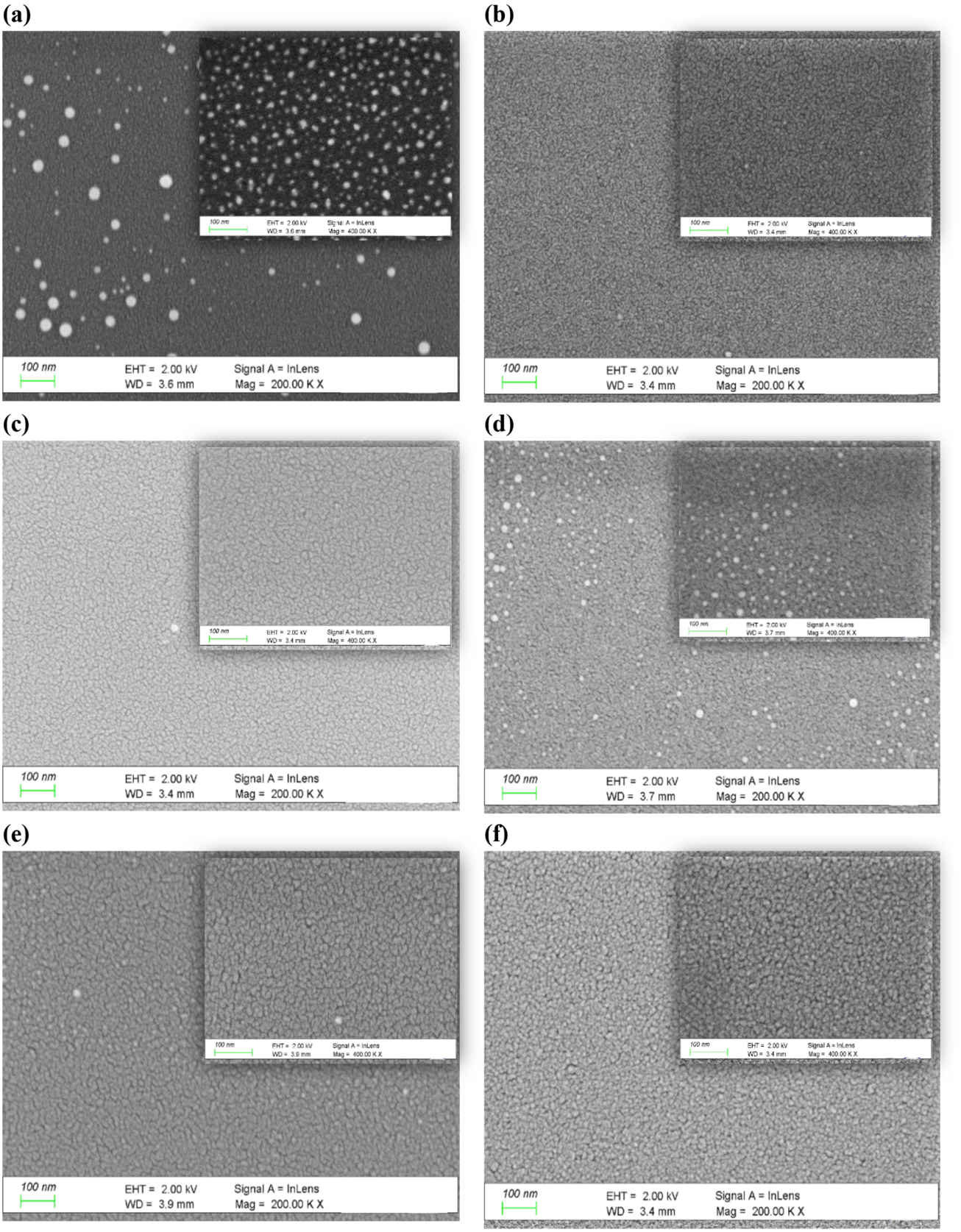

Figure 13. Surface morphology of unannealed MoO_3/Ir/MoO_3/Si (a−c) and postannealed (d−f) samples with different Ir thicknesses of 1, 2, and 4 respectively as observed under FESEM at different magnifications of 200 and 400 KX (inset).

performance and expand the range of applications for self-powered UV PDs. Detectivity (Figure 12a) provides a quantifiable measure of sensitivity by evaluating the device's ability to distinguish the desired UV signal from background

https://doi.org/10.1021/acsaelm.3c01047
ACS Appl. Electron. Mater. 2023, 5, 5696−5713

Table 2. Elemental Composition of Unannealed and Post-annealed MoO_3/Ir/MoO_3/Si Samples, While the Concentrations of All Elements Are Recorded in wt %

		presence of Si				absence of Si		
	samples	Si	O	Ir	Mo	O	Ir	Mo
unannealed	MoO_3/1 nm Ir/MoO_3/Si	97.0	1.5	1.2	0.4	40.0	50.4	9.6
	MoO_3/2 nm Ir/MoO_3/Si	94.9	1.7	2.7	0.7	28.5	63.1	8.5
	MoO_3/4 nm Ir/MoO_3/Si	93.2	1.9	4.1	0.8	24.3	24.3	6.7
post-annealed	MoO_3/1 nm Ir/MoO_3/Si	97.0	1.7	1.2	0.1	44.5	53.0	2.5
	MoO_3/2 nm Ir/MoO_3/Si	95.6	2.1	2.2	0.1	39.1	60.2	0.7
	MoO_3/4 nm Ir/MoO_3/Si	93.5	2.4	3.9	0.2	30.4	69.6	0.0

noise. Higher detectivity values, as observed for the post-annealed 2 nm Ir layer, indicate superior sensitivity and the capacity to detect weak UV signals while maintaining signal integrity amid the noise. The postannealed MoO_3/2 nm Ir/MoO_3/Si sample demonstrates an impressive detectivity value of 3.4×10^{11} Jones at 0 V bias. This high detectivity indicates the PD's exceptional sensitivity and ability to detect weak UV signals while minimizing the impact of background noise. The post-annealing process significantly contributes to achieving such a high detectivity by improving the crystalline structure, enhancing the quality of interfaces between layers, and optimizing overall device performance. These improvements effectively reduce noise levels, thereby increasing the signal-to-noise ratio and enabling the detection of even subtle UV signals with remarkable accuracy and reliability. The observed detectivity value of 3.4×10^{11} Jones underscores the outstanding performance of the post-annealed MoO_3/2 nm Ir/MoO_3/Si sample, highlighting its potential for demanding applications that require highly sensitive and efficient self-powered UV PD.

A higher EQE value (Figure 12b), such as the observed value of 132 for the post-annealed MoO_3/2 nm Ir/MoO_3/Si sample, indicates improved conversion efficiency and optimal utilization of incident UV light. This means that a larger proportion of incident UV photons is effectively converted into usable electrical current. Achieving a higher EQE value is crucial for high-performance self-powered UV PD as it ensures that a greater number of photons is successfully converted into electrical signals. This signifies excellent light absorption and charge generation capabilities in the device. By maximizing the utilization of incident UV light, the post-annealed MoO_3/2 nm Ir/MoO_3/Si sample demonstrates enhanced efficiency in capturing and utilizing the available light energy, resulting in a stronger and more reliable electrical output signal. The higher EQE value of 132 highlights the sample's exceptional performance in converting incident UV photons into usable electrical current, making it well-suited for demanding self-powered UV PD applications.

Surface Morphology and Elemental Composition. Figure 13a–c shows the FESEM of unannealed MoO_3/Ir/MoO_3/Si samples at 200 and 400 KX different magnifications of samples of MoO_3/1 nm Ir/MoO_3/Si, MoO_3/2 nm Ir/MoO_3/Si, and MoO_3/4 nm Ir/MoO_3/Si samples, respectively. For this case, at 1 nm Ir thickness, bigger particles are observed at low magnifications and increased at high magnifications. Those particles can be attributed to high distortion and scattering of the incent light and consequently will decrease the PD performances, as shown above in the electrical and optoelectronics sections. However, with increasing the thickness for 2 nm Ir, small porous structures started to appear. A similar case is observed at the 4 nm case with more porosity and more Ir content of 4 nm. In the 4 nm thickness, the conductivity increases dramatically, followed by 2 nm and then 1 nm cases. These results confirm the high optoelectronic properties of 4 nm Ir thick film.

The EQE, D^*, responsitivity, and response time values of 1 and 2 nm are somehow near each other. For the post-annealed MoO_3/Ir/MoO_3/Si samples with 1, 2, and 4 nm Ir thickness at different magnifications, the FESEM images are reported in Figure 13d–f. It is observed that the particles are a bit larger and denser after the postannealing process. At the same time, smoothing and homogeneity are presented here as well. Some very small particles are observed here, which are related to some agglomerations from the ALD tube lines that are related to MoO_3 particles. By comparing the unannealed and post-annealed samples for both groups, we can get an idea related to the effect of annealing on the morphological images. It is observed that for the unannealed MoO_3/1 nm Ir/MoO_3/Si, some particles are presented, but after the postannealed, these particles are enhanced and become smoother. This effect could directly affect the conductivity and optoelectronic properties, as shown from the optoelectronics measurements. The surface morphology of a PD can have a significant effect on its performance. The surface morphology can affect the absorption and scattering of light, the charge transport properties, and the surface photogenerated carrier concentrations. However, for the MoO_3/2 nm Ir/MoO_3/Si samples, we can observe small particles for both cases of unannealed and postannealed cases.

EDS analysis of the unannealed and post-annealed samples here is interesting as well to look at any changes in the composition and structures, as shown in Table 2. For the unannealed MoO_3/1, 2, and 4 nm Ir/MoO_3/Si, it is important to highlight that all the deposited MoO_3 layer is based on the same conditions in all Ir-based samples. The amount of Mo is 0.4, 0.7, and 0.8%; this increment is usually to balance the total amount of 100%. The Ir amounts are 1.2, 2.7, and 4.1%, as usual, because the deposited thickness is increased from 1, 2, and 4 nm over the whole surface. Moreover, for the O case, it is found 1.5, 1.7, and 1.9%. These results in the presence of Si peaks are normal, as expected before for the other samples. However, in the absence of a Si peak, the results show that Mo has 9.6, 8.5, and 6.7, which is decreasing logically as the Ir concentrations are increasing by 50.4, 63.1, and 69.0% for the O concentrations 40.0, 28.5, and 24.3%. On the other hand, for the post-annealed MoO_3/Ir/MoO_3/Si with 1, 2, and 4 nm Ir thickness, it is also interesting to look at the elemental analysis. First, in the presence of Si peaks, the Mo concentrations are almost the same at 0.1, 0.1, and 0.2%. The Ir contents are about 1.2, 2.2, and 3.9%. It may refer to these results, which enhanced the presence and crystallinity of MoO_3/Ir layer/MoO_3 for better PD performance. For the O contents, 1.7, 2.1, and 2.4%. On the other hand, by looking at the concentrations of these elements of the unannealed MoO_3/Ir/MoO_3/Si samples, we found that the detected amount of Mo

https://doi.org/10.1021/acsaelm.3c01047
ACS Appl. Electron. Mater. 2023, 5, 5696–5713

Table 3. Roughness Measurement of Unannealed and Post-annealed MoO_3/Ir/MoO_3/Si with 1, 2, and 4 nm Ir Thickness[a]

	sample	min (nm)	max (nm)	mid (nm)	R_{pv}(nm)	R_q(nm)	R_a(nm)	R_z(nm)	R_{sk}	R_{ku}
unannealed	MoO_3/1 nmIr/MoO_3/Si	−0.57	0.44	−0.06	1.01	0.19	0.16	0.79	0.23	2.66
	MoO_3/2 nmIr/MoO_3/Si	−0.89	0.80	−0.04	1.69	0.32	0.25	1.33	−0.03	3.04
	MoO_3/4 nmIr/MoO_3/Si	−4.39	4.52	0.07	8.91	2.22	1.81	8.59	−0.21	2.29
post-annealed	MoO_3/1 nmIr/MoO_3/Si	−1.43	1.20	−0.12	2.64	0.54	0.43	2.28	0.01	2.57
	MoO_3/2 nmIr/MoO_3/Si	−0.75	1.21	0.22	1.98	0.35	0.28	1.29	−0.25	3.13
	MoO_3/4 nmIr/MoO_3/Si	−6.68	6.53	−0.08	13.21	3.26	2.63	12.13	0.087	2.21

[a]The measurements were taken through a horizontal line.

was 0.4, 0.7, and 0.8%, the Ir was 1.2, 2.7, and 4.1%, and finally, the O amounts were 1.5, 1.7, and 1.9%. Comparing the results of the unannealed and the post-annealed samples, we found that the concentration of Mo decreased, Ir decreased, and O increased, the excess of the oxidation of the Si substrate. On the other hand, in the absence of Si peaks, Mo is 2.5, 0.7, and 0%, Ir is 53.0, 60.2, and 69.6%, and O is 44.5, 39.1, and 30.4%. The contents of Mo decreased, Ir increased, and the contents of O decreased.

Surface Topography and Roughness. In the field of surface metrology and topography, various parameters are utilized to characterize the topography of a surface. These parameters offer valuable insights into the surface's features and irregularities. One such parameter is the average roughness (R_a) that represents the arithmetic mean of surface heights within a defined area. It provides a measure of the overall surface roughness. The root means square of the height values (R_q) is another parameter that quantifies the deviation of height values from the mean, indicating the surface's overall variation. The height difference or peak-to-valley distance (R_{pv}) measures the vertical span between the highest peak and the lowest valley on the surface, reflecting the extent of surface irregularities. Additionally, the ten-point height (R_z) parameter is used to calculate the average height of the five highest peaks and the five lowest valleys on the surface, providing a measure of localized surface features. Furthermore, parameters such as skewness (R_{sk}) and kurtosis (R_{ku}) describe the asymmetry and sharpness of the surface features, respectively. These parameters collectively provide a comprehensive description of the surface topography, facilitating quantitative analysis and comparison. A summary of these parameters for both annealed and post-annealed samples can be found in Table 3, while the 3D images are presented in Figures S4 and S5 (Supporting Information). The AFM analysis of the unannealed and post-annealed MoO_3/Ir/MoO_3/Si samples provides valuable insights into their surface characteristics. A comparison between the two chromatographs reveals notable differences. The post-annealed samples exhibit slightly higher values for R_{pv}, R_q, and R_a compared to the unannealed samples, suggesting surface modifications induced by the annealing process and increased roughness. However, despite the increase in roughness, the post-annealed samples demonstrate improved performance as high-performance PDs. This suggests that factors beyond surface roughness, such as interface quality, defect reduction, and carrier transport, are crucial to determining PD performance. It is important to note that even with the slight increase in roughness, the post-annealed samples show significant enhancements in detectivity and EQE values. For instance, the MoO_3/2 nm Ir/MoO_3/Si sample exhibits a detectivity value of 3.4×10^{11} Jones and an EQE value of 132 at 0 V bias. These findings highlight the importance of optimizing various parameters to achieve high-performance self-powered PD. Interestingly, Table S2 (Supporting Information) shows the AFM surface topography parameters of the Ir/Si device of 1, 2, and 4 nm Ir layer. Notably, the 1 nm Ir sample exhibited the lowest roughness of 0.29 nm, indicating a highly smooth and uniform surface.

CONCLUSIONS

In conclusion, this study investigates the performance of self-powered photodetectors based on α-MoO_3/Ir/α-MoO_3 structures after post-annealing. The annealing process significantly improves optoelectronic properties, enabling negative photoconductivity at a 0 V bias voltage. Notably, this study demonstrates the first instance of a MoO_3-based UV photodetector exhibiting a negative response with higher detectivity compared to the unannealed counterpart. The device achieves a rapid 0.2 ms response time at a 0 V bias, highlighting its suitability for high-speed applications. Furthermore, the study reveals the superior performance of 1 and 2 nm Ir layers in terms of photocurrent generation, light sensitivity, and switching behavior, while the 4 nm Ir layer exhibits weaker performance. The interplay between different layers in the MoO_3/Ir/MoO_3 structures and the role of oxygen vacancies are elucidated, with the oxygen vacancies acting as trap-assisted conduction centers that reduce carrier density and lead to negative photoconductivity. These findings highlight the potential of nanostructured MoO_3/Ir heterostructures for high-performance self-powered photodetectors, contributing to advancements in transparent optoelectronics, integrated photonic systems, and energy harvesting technologies.

ASSOCIATED CONTENT

Data Availability Statement

The data presented in this study can be obtained upon request from the corresponding author.

Supporting Information

The Supporting Information is available free of charge at https://pubs.acs.org/doi/10.1021/acsaelm.3c01047.

Additional experimental details for enhanced photodetector performance and characterization.

Supplementary figures and tables for a deeper understanding of the study.

Figure S1: comparative OFF-ON performance of both unannealed and postannealed MoO3/Ir/MoO3/Si photodetectors across bias voltages of 0, 0.5, 1, 2, 3, 4, and 5 V; Figure S2: assessment of mobility and carrier concentration in unannealed and postannealed MoO3/Ir/MoO3/Si samples; Figure S3: diffuse reflectance measurements for unannealed and post-annealed MoO3/Ir/MoO3/Si samples; Figure S4: three-dimensional topography depiction along with line profiles of the unannealed MoO3/Ir/MoO3/Si device; Figure S5: three-dimensional topography visualization along with

https://doi.org/10.1021/acsaelm.3c01047
ACS Appl. Electron. Mater. 2023, 5, 5696−5713

line profiles of the post-annealed MoO3/Ir/MoO3/Si device; figure S6: responsivity as a function of applied bias voltages of 0, 0.5, 1, 2, 3, 4, and 5 V for unannealed and post-annealed MoO3/Ir/MoO3/Si thin films under a UV 365 nm wavelength light source; Table S1: compilation of electrical Hall effect measurements for Ir/Si samples with 1, 2, and 4 nm Ir layers; Table S2: AFM surface topographical parameters of Ir/Si device with 1, 2, and 4 nm Ir layers (PDF)

AUTHOR INFORMATION

Corresponding Author

Mohamed A. Basyooni − *Department of Nanotechnology and Advanced Materials, Graduate School of Applied and Natural Science, Selçuk University, Konya 42030, Turkey; Department of Precision and Microsystems Engineering, Delft University of Technology, 2628 CD Delft, Netherlands;* orcid.org/0000-0001-8473-8253; Email: m.a.basyooni@gmail.com, m.kabatas@tudelft.nl

Authors

Mohammed Tihtih − *Institute of Ceramics and Polymer Engineering, University of Miskolc, H-3515 Miskolc, Hungary;* orcid.org/0000-0001-7364-9036

Shrouk E. Zaki − *Department of Nanotechnology and Advanced Materials, Graduate School of Applied and Natural Science, Selçuk University, Konya 42030, Turkey;* orcid.org/0000-0002-5097-1070

Yasin Ramazan Eker − *Department of Basic Sciences, Faculty of Engineering and Science and Technology Research and Application Center (BITAM), Necmettin Erbakan University, Konya 42090, Turkey;* orcid.org/0000-0001-7395-4364

Complete contact information is available at: https://pubs.acs.org/10.1021/acsaelm.3c01047

Notes

The authors declare no competing financial interest.

ACKNOWLEDGMENTS

The authors would like to express their gratitude to the Selçuk University-Scientific Research Projects Coordination (BAP) Unit for their support under grant number 22211012. Additionally, the authors acknowledge the continuous support provided by Necmettin Erbakan University-Science and Technology Research and Application Center (BITAM) during the characterization sections.

REFERENCES

(1) Yadav, P. K.; Ajitha, B.; Reddy, Y. A. K.; Sreedhar, A. Recent advances in development of nanostructured photodetectors from ultraviolet to infrared region: A review. *Chemosphere* **2021**, *279*, No. 130473.

(2) Schneider, W. Theory of the negative photoconductivity in crossed fields. *Appl. Phys.* **1976**, *11*, 141−146.

(3) Novikov, V.; Sturman, B. Theory of an absolute negative photoconductivity of ruby. *Zh. Eksp. Teor. Fiz.* **1988**, *94*, 238.

(4) Bräunlich, P. Possibility of Observing Negative Thermally Stimulated Conductivity. *J. Appl. Phys.* **1968**, *39* (6), 2953−2956.

(5) Ryzhii, V.; Ryzhii, M.; Ponomarev, D.; Leiman, V.; Mitin, V.; Shur, M.; Otsuji, T. Negative photoconductivity and hot-carrier bolometric detection of terahertz radiation in graphene-phosphorene hybrid structures. *J. Appl. Phys.* **2019**, *125* (15), 151608.

(6) Jones, B.; Beaudet, P. Negative photoconductivity and electrical instabilities in semiconductors. *Can. J. Phys.* **1967**, *45* (12), 4091−4101.

(7) Novikov, V.; Sturman, B. Negative hopping photoconductivity in lattice models. *J. Phys. C: Solid State Phys.* **1987**, *20* (29), 4845.

(8) Malinovsky, V.; Novikov, V.; Sturman, B. Mechanisms of absolute negative photoconductivity in solids. *Phys. Lett. A* **1985**, *112* (5), 237−239.

(9) Malinovskii, V.; Novikov, V.; Sturman, B. Mechanisms for the absolute negative photoconductivity of insulators. *J. Exp. Theor. Phys. Lett.* **1985**, *41* (7), 349−352.

(10) Kunz, R.; Schöll, E. Bistability and negative photoconductivity in optically induced real-space transfer. *Phys. Rev. B* **1993**, *47* (8), 4337.

(11) Basyooni, M. A.; Belaid, W.; Houimi, A.; Zaki, S. E.; Eker, Y. R.; Gezgin, S. Y.; Kiliç, H. Ş. Observation of negative photoresponse in joule-heated Au/Cu2SnS3 ternary chalcogenide thin film deposited by low energy pulsed laser deposition. *Opt. Mater.* **2022**, *128*, No. 112389.

(12) Yang, Y.; Peng, X.; Kim, H.-S.; Kim, T.; Jeon, S.; Kang, H. K.; Choi, W.; Song, J.; Doh, Y.-J.; Yu, D. Hot carrier trapping induced negative photoconductance in InAs nanowires toward novel non-volatile memory. *Nano Lett.* **2015**, *15* (9), 5875−5882.

(13) Beaulieu, Y.; Webb, J.; Brebner, J. Hot electron induced negative photoconductivity in n-InSb/GaAs with above gap illumination at low temperature. *Solid State Commun.* **1990**, *76* (3), 233−236.

(14) Kimura, H.; Kurosu, T.; Akiba, Y.; Iida, M. A model for the occurrence of transient negative photoconductivity in silicon doped with gold. *Appl. Phys. A: Mater. Sci. Process.* **1991**, *53*, 194−197.

(15) Liu, Y.; Fu, P.; Yin, Y.; Peng, Y.; Yang, W.; Zhao, G.; Wang, W.; Zhou, W.; Tang, D. Positive and negative photoconductivity conversion induced by H2O molecule adsorption in WO3 nanowire. *Nanoscale Res. Lett.* **2019**, *14* (1), 1−7.

(16) Wang, Q.; Tu, Y.; Ichii, T.; Utsunomiya, T.; Sugimura, H.; Hao, L.; Wang, R.; He, X. Decoration of reduced graphene oxide by gold nanoparticles: an enhanced negative photoconductivity. *Nanoscale* **2017**, *9* (38), 14703−14709.

(17) Zhuang, S.; Chen, Y.; Xia, Y.; Tang, N.; Xu, X.; Hu, J.; Chen, Z. Coexistence of negative photoconductivity and hysteresis in semiconducting graphene. *AIP Adv.* **2016**, *6* (4), No. 045214.

(18) Haque, M. A.; Li, J. L.; Abdelhady, A. L.; Saidaminov, M. I.; Baran, D.; Bakr, O. M.; Wei, S. H.; Wu, T. Transition from positive to negative photoconductance in doped hybrid perovskite semiconductors. *Adv. Opt. Mater.* **2019**, *7* (22), 1900865.

(19) Lui, C.; Frenzel, A.; Pilon, D.; Lee, Y.-H.; Ling, X.; Akselrod, G.; Kong, J.; Gedik, N. Trion-induced negative photoconductivity in monolayer MoS 2. *Phys. Rev. Lett.* **2014**, *113* (16), No. 166801.

(20) Yuan, Y.; Yao, Q.; Zhang, J.; Wang, K.; Zhang, W.; Zhou, T.; Sun, H.; Ding, J. Negative photoconductivity in Cs 4 PbBr 6 single crystal. *Phys. Chem. Chem. Phys.* **2020**, *22* (25), 14276−14283.

(21) Tailor, N. K.; Maity, P.; Satapathi, S. Observation of Negative Photoconductivity in Lead-Free Cs3Bi2Br9Perovskite Single Crystal. *ACS Photonics* **2021**, *8* (8), 2473−2480.

(22) Tailor, N. K.; Maity, P.; Saidaminov, M. I.; Pradhan, N.; Satapathi, S. Dark self-healing-mediated negative photoconductivity of a lead-free Cs3Bi2Cl9 perovskite single crystal. *J. Phys. Chem. Lett.* **2021**, *12* (9), 2286−2292.

(23) Vardi, A.; Bahir, G.; Schacham, S.; Kandaswamy, P.; Monroy, E. Negative photoconductivity due to intraband transitions in GaN/AlN quantum dots. *J. Appl. Phys.* **2010**, *108* (10), 104512.

(24) Yang, J.; Li, R.; Huo, N.; Ma, W.-L.; Lu, F.; Fan, C.; Yang, S.; Wei, Z.; Li, J.; Li, S.-S. Oxygen-induced abnormal photoelectric behavior of a MoO 3/graphene heterocomposite. *RSC Adv.* **2014**, *4* (91), 49873−49878.

(25) Tavares, M.; da Silva, M.; Peres, M.; de Castro, S.; Soares, D.; Okazaki, A.; Fornari, C.; Rappl, P.; Abramof, E. Investigation of negative photoconductivity in p-type Pb1-xSnxTe film. *Appl. Phys. Lett.* **2017**, *110* (4), No. 042102.

(26) Grillo, A.; Faella, E.; Pelella, A.; Giubileo, F.; Ansari, L.; Gity, F.; Hurley, P. K.; McEvoy, N.; Di Bartolomeo, A. Coexistence of negative and positive photoconductivity in few-layer PtSe2 field-effect transistors. *Adv. Funct. Mater.* **2021**, *31* (43), 2105722.

(27) Vargas, L. M.; de Castro, S.; Peres, M. L.; de Godoy, M. P.; Soares, D. A. Tuning positive and negative photoconductivity in Zn1-xCdxO films. *J. Alloys Compd.* **2018**, *749*, 734−740.
(28) Qin, J.-X.; Yang, X.-G.; Lv, C.-F.; Li, Y.-Z.; Chen, X.-X.; Zhang, Z.-F.; Zang, J.-H.; Yang, X.; Liu, K.-K.; Dong, L. Humidity sensors realized via negative photoconductivity effect in nanodiamonds. *J. Phys. Chem. Lett.* **2021**, *12* (16), 4079−4084.
(29) Zhuang, S.; Chen, Y.; Zhang, W.; Chen, Z.; Wang, Z. Humidity sensor and ultraviolet photodetector based on carrier trapping effect and negative photoconductivity in graphene quantum dots. *Sci. China: Phys., Mech. Astron.* **2018**, *61*, No. 014211.
(30) Hassan, M. Y.; Ang, D. S. On-demand visible-light sensing with optical memory capabilities based on an electrical-breakdown-triggered negative photoconductivity effect in the ubiquitous transparent Hafnia. *ACS Appl. Mater. Interfaces* **2019**, *11* (45), 42339−42348.
(31) Singh, S. C.; Peng, Y.; Rutledge, J.; Guo, C. Photothermal and Joule-heating-induced negative-photoconductivity-based ultraresponsive and near-zero-biased copper selenide photodetectors. *ACS Appl. Electron. Mater.* **2019**, *1* (7), 1169−1178.
(32) Xie, L.; Guo, L.; Yu, W.; Kang, T.; Zheng, R.-K.; Zhang, K. Ultrasensitive negative photoresponse in 2D Cr2Ge2Te6 photodetector with light-induced carrier trapping. *Nanotechnology* **2018**, *29* (46), 464002.
(33) Wort, C. J.; Balmer, R. S. Diamond as an electronic material. *Mater. Today* **2008**, *11* (1−2), 22−28.
(34) Dang, Q.; Lin, H.; Fan, Z.; Ma, L.; Shao, Q.; Ji, Y.; Zheng, F.; Geng, S.; Yang, S.-Z.; Kong, N. Iridium metallene oxide for acidic oxygen evolution catalysis. *Nat. Commun.* **2021**, *12* (1), 6007.
(35) Ping, Y.; Nielsen, R. J.; Goddard, W. A., III The reaction mechanism with free energy barriers at constant potentials for the oxygen evolution reaction at the IrO2 (110) surface. *J. Am. Chem. Soc.* **2017**, *139* (1), 149−155.
(36) Liu, H.; Yang, R. B.; Yang, W.; Jin, Y.; Lee, C. J. Atomic layer deposition and post-growth thermal annealing of ultrathin MoO3 layers on silicon substrates: Formation of surface nanostructures. *Appl. Surf. Sci.* **2018**, *439*, 583−588.
(37) Diskus, M.; Nilsen, O.; Fjellvåg, H. Growth of thin films of molybdenum oxide by atomic layer deposition. *J. Mater. Chem.* **2011**, *21* (3), 705−710.
(38) Mattinen, M.; King, P. J.; Khriachtchev, L.; Heikkilä, M. J.; Fleming, B.; Rushworth, S.; Mizohata, K.; Meinander, K.; Räisänen, J.; Ritala, M. Atomic layer deposition of crystalline molybdenum oxide thin films and phase control by post-deposition annealing. *Mater. Today Chem.* **2018**, *9*, 17−27.
(39) Pavlovic, Z.; Ranjan, C.; van Gastel, M.; Schlögl, R. The active site for the water oxidising anodic iridium oxide probed through in situ Raman spectroscopy. *Chem. Commun.* **2017**, *53* (92), 12414−12417.
(40) Liao, P.; Chen, C.; Ho, W.; Huang, Y.; Tiong, K.-K. Characterization of IrO2 thin films by Raman spectroscopy. *Thin Solid Films* **1997**, *301* (1−2), 7−11.
(41) Kim, J. H.; Dash, J. K.; Kwon, J.; Hyun, C.; Kim, H.; Ji, E.; Lee, G.-H. van der Waals epitaxial growth of single crystal α-MoO3 layers on layered materials growth templates. *2D Mater.* **2019**, *6* (1), No. 015016.
(42) Xie, W.; Su, M.; Zheng, Z.; Wang, Y.; Gong, L.; Xie, F.; Zhang, W.; Luo, Z.; Luo, J.; Liu, P. Nanoscale insights into the hydrogenation process of layered α-MoO3. *ACS Nano* **2016**, *10* (1), 1662−1670.
(43) Wang, Y.; Du, X.; Wang, J.; Su, M.; Wan, X.; Meng, H.; Xie, W.; Xu, J.; Liu, P. Growth of large-scale, large-size, few-layered α-MoO3 on SiO2 and its photoresponse mechanism. *ACS Appl. Mater. Interfaces* **2017**, *9* (6), 5543−5549.
(44) Zheng, B.; Wang, Z.; Chen, Y.; Zhang, W.; Li, X. Centimeter-sized 2D α-MoO3 single crystal: growth, Raman anisotropy, and optoelectronic properties. *2D Mater.* **2018**, *5* (4), No. 045011.
(45) Arash, A.; Ahmed, T.; Rajan, A. G.; Walia, S.; Rahman, F.; Mazumder, A.; Ramanathan, R.; Sriram, S.; Bhaskaran, M.; Mayes, E. Large-area synthesis of 2D MoO3− x for enhanced optoelectronic applications. *2D Mater.* **2019**, *6* (3), No. 035031.
(46) Harutyunyan, H.; Martinson, A. B.; Rosenmann, D.; Khorashad, L. K.; Besteiro, L. V.; Govorov, A. O.; Wiederrecht, G. P. Anomalous ultrafast dynamics of hot plasmonic electrons in nanostructures with hot spots. *Nat. Nanotechnol.* **2015**, *10* (9), 770−774.
(47) Schets, H.; Janssen, P.; Witters, J.; Borghs, S. Negative persistent photoconductivity in an InAs/GaSb quantum well. *Solid State Commun.* **1999**, *110* (3), 169−171.
(48) Sadofyev, Y. G.; Ramamoorthy, A.; Bird, J.; Johnson, S. R.; Zhang, Y.-H. Large negative persistent photoconductivity in InAs/AlSb quantum wells. *Appl. Phys. Lett.* **2005**, *86* (19), 192109.
(49) Chafai, M.; Jaouhari, A.; Torres, A.; Antón, R.; Martın, E.; Jiménez, J.; Mitchel, W. Raman scattering from LO phonon-plasmon coupled modes and Hall-effect in n-type silicon carbide 4H−SiC. *J. Appl. Phys.* **2001**, *90* (10), 5211−5215.
(50) Zhang, X.-Y.; Han, D.; Ma, N.; Gao, R.; Zhu, A.; Guo, S.; Zhang, Y.; Wang, Y.; Yang, J.; Chen, L. Carrier density-dependent localized surface plasmon resonance and charge transfer observed by controllable semiconductor content. *J. Phys. Chem. Lett.* **2018**, *9* (20), 6047−6051.
(51) Liu, S.; Yang, Z.; Zhao, L.; Zhang, Y.; Xing, Y.; Fei, T.; Zhang, H.; Zhang, T. Glucose-assisted combustion synthesis of oxygen vacancy enriched α-MoO3 for ethanol sensing. *J. Alloys Compd.* **2022**, *902*, No. 163711.
(52) Wu, Q.-L.; Zhao, S.-X.; Yu, L.; Zheng, X.-X.; Wang, Y.-F.; Yu, L.-Q.; Nan, C.-W.; Cao, G. Oxygen vacancy-enriched MoO 3− x nanobelts for asymmetric supercapacitors with excellent room/low temperature performance. *J. Mater. Chem. A* **2019**, *7* (21), 13205−13214.
(53) Wang, H.; Wang, F.; Xu, T.; Xia, H.; Xie, R.; Zhou, X.; Ge, X.; Liu, W.; Zhu, Y.; Sun, L. Slowing hot-electron relaxation in mix-phase nanowires for hot-carrier photovoltaics. *Nano Lett.* **2021**, *21* (18), 7761−7768.
(54) Zhang, T.-F.; Li, Z.-P.; Wang, J.-Z.; Kong, W.-Y.; Wu, G.-A.; Zheng, Y.-Z.; Zhao, Y.-W.; Yao, E.-X.; Zhuang, N.-X.; Luo, L.-B. Broadband photodetector based on carbon nanotube thin film/single layer graphene Schottky junction. *Sci. Rep.* **2016**, *6* (1), 38569.
(55) Yamada, K.; Nishikubo, R.; Oga, H.; Ogomi, Y.; Hayase, S.; Kanno, S.; Imamura, Y.; Hada, M.; Saeki, A. Anomalous dielectric behavior of a Pb/Sn perovskite: effect of trapped charges on complex photoconductivity. *Acs Photonics* **2018**, *5* (8), 3189−3197.
(56) He, Q.; Chen, G.; Wang, Y.; Liu, X.; Xu, D.; Xu, X.; Liu, Y.; Bao, J.; Wang, X. CsPbX3-ITO (X= Cl, Br, I) Nano-Heterojunctions: Voltage Tuned Positive to Negative Photoresponse. *Small* **2021**, *17* (28), 2101403.
(57) Li, J.-L.; Yang, J.; Wu, T.; Wei, S.-H. Formation of DY center as n-type limiting defects in octahedral semiconductors: the case of Bi-doped hybrid halide perovskites. *J. Mater. Chem. C* **2019**, *7* (14), 4230−4234.
(58) Jin, H.; Chen, Y.; Zhang, L.; Wan, R.; Zou, Z.; Li, H.; Gao, Y. Positive and negative photoconductivity characteristics in CsPbBr3/graphene heterojunction. *Nanotechnology* **2021**, *32* (8), No. 085202.
(59) Biswas, C.; Güneş, F.; Loc, D. D.; Lim, S. C.; Jeong, M. S.; Pribat, D.; Lee, Y. H. Negative and positive persistent photoconductance in graphene. *Nano Lett.* **2011**, *11* (11), 4682−4687.
(60) Gao, Y.; Lei, S.; Kang, T.; Fei, L.; Mak, C.-L.; Yuan, J.; Zhang, M.; Li, S.; Bao, Q.; Zeng, Z. Bias-switchable negative and positive photoconductivity in 2D FePS3 ultraviolet photodetectors. *Nanotechnology* **2018**, *29* (24), 244001.
(61) Wang, Q.; Guo, X.; Cai, L.; Cao, Y.; Gan, L.; Liu, S.; Wang, Z.; Zhang, H.; Li, L. TiO 2-decorated graphenes as efficient photoswitches with high oxygen sensitivity. *Chem. Sci.* **2011**, *2* (9), 1860−1864.
(62) Zheng, K.; Meng, F.; Jiang, L.; Yan, Q.; Hng, H. H.; Chen, X. Visible photoresponse of single-layer graphene decorated with TiO2 nanoparticles. *Small* **2013**, *9* (12), 2076−2080.
(63) Lin, Z.; Guo, C.; Fu, Q.; Song, W. Abnormal photoelectrical properties and gas sensing of mesoporous Sn0. 9Ti0. 1O2 film under UV light. *Mater. Lett.* **2013**, *102*, 47−49.
(64) Cai, P.; Chen, J.; Ding, Y.; Liu, Y.; Wen, Z. Defect-rich MoO3 nanobelt cathode for a high-performance hybrid alkali/acid Zn-MoO3 rechargeable battery. *ACS Sustainable Chem. Eng.* **2021**, *9* (34), 11524−11533.

https://doi.org/10.1021/acsaelm.3c01047
ACS Appl. Electron. Mater. 2023, 5, 5696−5713

(65) Apergi, S.; Koch, C.; Brocks, G.; Olthof, S.; Tao, S. Decomposition of Organic Perovskite Precursors on MoO3: Role of Halogen and Surface Defects. *ACS Appl. Mater. Interfaces* **2022**, *14* (30), 34208−34219.
(66) Wu, Y.; Wang, H.; Tu, W.; Wu, S.; Chew, J. W. Construction of hole-transported MoO3-x coupled with CdS nanospheres for boosting photocatalytic performance via oxygen-defects-mediated Z-scheme charge transfer. *Appl. Organomet. Chem.* **2019**, *33* (4), No. e4780.
(67) Chu, Q.; Li, J.; Jin, S.; Guo, S.; Park, E.; Wang, J.; Chen, L.; Jung, Y. M. Charge-transfer induced by the oxygen vacancy defects in the Ag/MoO3 composite system. *Nanomaterials* **2021**, *11* (5), 1292.
(68) Jagadeeswararao, M.; Sim, K. M.; Lee, S.; Kang, M.; An, S.; Nam, G.-H.; Sim, H. R.; Oleiki, E.; Lee, G.; Chung, D. S. Stoichiometric Engineering of Cs2AgBiBr6 for Photomultiplication-Type Photodetectors. *Chem. Mater.* **2023**, *35* (8), 3095−3104.
(69) Ho, L. T. T.; Mukherjee, A.; Vasileska, D.; Akis, J.; Stavro, J.; Zhao, W.; Goldan, A. H. Modeling Dark Current Conduction Mechanisms and Mitigation Techniques in Vertically Stacked Amorphous Selenium-Based Photodetectors. *ACS Appl. Electron. Mater.* **2021**, *3* (8), 3538−3546.
(70) Makhlouf, M.; Khallaf, H.; Shehata, M. Impedance spectroscopy and transport mechanism of molybdenum oxide thin films for silicon heterojunction solar cell application. *Appl. Phys. A: Mater. Sci. Process.* **2022**, *128* (2), 98.
(71) Razmyar, S.; Sheng, T.; Akter, M.; Zhang, H. Low-temperature photocatalytic hydrogen addition to two-dimensional MoO3 nanoflakes from isopropyl alcohol for enhancing solar energy harvesting and conversion. *ACS Appl. Nano Mater.* **2019**, *2* (7), 4180−4192.
(72) Wang, H.; Guan, N.; Feng, Z.; Xiang, W.; Zhao, H.; Zhang, X. Constructing defect engineered 2D/2D MoO3/g-C3N4 Z-scheme heterojunction for enhanced photocatalytic activity. *J. Alloys Compd.* **2022**, *926*, No. 166964.
(73) Dai, J.; Qi, X.; Xia, L.; Xue, Q.; Luo, L.; Wang, X.; Yang, C.; Li, D.; Xie, H.; Cabot, A. Aqueous ammonium-ion supercapacitors with unprecedented energy density and stability enabled by oxygen vacancy-enriched MoO3@ C. *Adv. Funct. Mater.* **2023**, *33* (10), 2212440.
(74) Tang, B.; Li, W.; Zhang, X.; Zhang, B.; Zhang, H.; Li, C. Depolymerization of Kraft lignin to liquid fuels with MoS2 derived oxygen-vacancy-enriched MoO3 in a hydrogen-donor solvent system. *Fuel* **2022**, *324*, No. 124674.
(75) Hajnal, Z.; Miró, J.; Kiss, G.; Réti, F.; Deák, P.; Herndon, R. C.; Kuperberg, J. M. Role of oxygen vacancy defect states in the n-type conduction of β-Ga2O3. *J. Appl. Phys.* **1999**, *86* (7), 3792−3796.
(76) Li, S.; Yue, J.; Ji, X.; Lu, C.; Yan, Z.; Li, P.; Guo, D.; Wu, Z.; Tang, W. Oxygen vacancies modulating the photodetector performances in ε-Ga2O3 thin films. *J. Mater. Chem. C* **2021**, *9* (16), 5437−5444.

https://doi.org/10.1021/acsaelm.3c01047
ACS Appl. Electron. Mater. 2023, 5, 5696−5713